Tectonic evolution records closure of the Western Kunlun–Pamir Paleo-Tethys Realm: Insights from provenance analyses of Jurassic siliciclastic strata

Hang Cui[1,2,3], Shifa Zhu[1,2,†], Nigel P. Mountney[3], Adam McArthur[3], Jianzhou Tang[4], Yao Dong[1,2], Yihu Suo[1,2], Huan Tong[1,2], and Xianzhang Yang[5]

[1]*State Key Laboratory of Petroleum Resources and Engineering, China University of Petroleum (Beijing), Beijing 102249, China*
[2]*College of Geosciences, China University of Petroleum, Beijing 102249, China*
[3]*Sedimentology Research Group, School of Earth and Environment, University of Leeds, Leeds LS2 9JT, UK*
[4]*College of Geology and Environment, Xi'an University of Science and Technology, Xi'an 710054, China*
[5]*Research Institute of Petroleum Exploration and Development, Tarim Oilfield Company, PetroChina, Korla 841000, China*

ABSTRACT

Determining the provenance history of Jurassic sediments in the southwestern Tarim Basin is crucial for deciphering the tectonic evolution of the Western Kunlun–Pamir Paleo-Tethys Realm, which forms the northwesternmost segment of the Himalayan-Tibetan Plateau. Yet, the detailed spatial provenance variation of these strata is poorly constrained. This study integrates field observations from three outcropping sections (cumulative thickness of ~6800 m) and three wells (~3600 m) from four distinct regions: Qimgan, Oytag, Toyunduk-Kyzyltau, and Fusha. Samples were collected for analysis of sandstone petrology (n = 54), heavy mineral assemblages (n = 18), and detrital zircon U-Pb geochronology (n = 10) to delineate the spatial differences in Jurassic provenance. The results indicate that the southwestern Tarim Basin can be demarcated into two tectonic domains: (1) Detrital zircons in the Qimgan and Oytag regions were predominantly derived from nearby Triassic backarc volcanic rocks. Additionally, late Paleozoic subpopulations were sourced from a volcanic sequence exposed in the northeastern part of North Pamir Terrane, induced by Carboniferous–Permian Paleo-Tethys subduction. North Pamir Terrane served as the main elevated source area, with negligible contributions from Central and/or South Pamir terranes. (2) The detrital zircons of early

Paleozoic and Neoproterozoic ages from the Toyunduk-Kyzyltau and Fusha regions predominantly originated from the North Kunlun and South Kunlun terranes in response to Triassic collisional orogeny that induced significant uplift, effectively disconnecting the more distant provenance areas of the Tianshuihai and/or Songpan-Ganzi terranes. Insights from provenance analysis permit the delineation of a refined geodynamic model for the tectonic evolution of the closure of the Western Kunlun–Pamir Paleo-Tethys Realm. This study demonstrates Triassic backarc volcanism in the northeastern Chinese Pamir region, which supports a previously proposed hypothesis. These findings not only deepen our insights into the tectonic evolution of the Western Kunlun–Pamir Paleo-Tethys Realm but also significantly enhance our understanding of the dynamics of sedimentary basins, crustal development, and resource prospecting within convergent orogenic settings.

INTRODUCTION

The Himalayan-Tibetan orogen represents a composite terrane that was assembled through a series of collisional events and accretion along the southern periphery of the Asian continent (Fig. 1A), culminating in the present configuration between India and Eurasia (e.g., Windley, 1983; Kellett and Grujic, 2012; Metcalfe, 2021). Situated at the northwesternmost extent of the Himalayan-Tibetan Plateau, the Western Kunlun Shan–Pamir Realm has undergone a complex geodynamic evolution, characterized by the sequential origin, expansion, and closure of various branches of the Proto-, Paleo-, and

Neo-Tethys oceans. Evidence for reconstructing this evolutionary history is encapsulated in the remnant crustal fragments juxtaposed against a variety of volcanic arcs and suture zones (e.g., Gibbons et al., 2015; Liu et al., 2020; Tang et al., 2021), which provide critical insights into the origin and formation of the Central Asian Orogenic Belt.

The region's significance surpasses its geological complexity. From a topographical and tectonic perspective, the contemporary Western Kunlun Shan–Pamir Realm epitomizes intracontinental collision and serves as a pivotal regulator of atmospheric composition exchange, thereby influencing regional and global climate patterns (e.g., Bershaw et al., 2012; Blayney et al., 2016). Understanding its geological history is thus essential for deciphering past climate dynamics. Despite considerable research devoted to the Cenozoic differential uplift history and the dynamic mechanisms of the Western Kunlun Shan–Pamir Realm (e.g., Sobel et al., 2013; Xu et al., 2021), its pre-Cenozoic tectonic evolution remains relatively poorly constrained. This knowledge gap is predominantly due to the profound overprinting of pre-Cenozoic geological processes by the Cenozoic tectonic evolution of the Pamir Plateau (e.g., Bershaw et al., 2012). Addressing this gap is vital for achieving a holistic understanding of continental growth, basin evolution, and orogenic processes.

Research into the Mesozoic geodynamic history of the Western Kunlun Shan–Pamir Realm has focused on the genesis of igneous and metamorphic sequences exposed within or in proximity to sutures and plutons (e.g., Wang et al., 2020; Tang et al., 2021; Liu et al., 2023). Although the fieldwork itself is not difficult, the

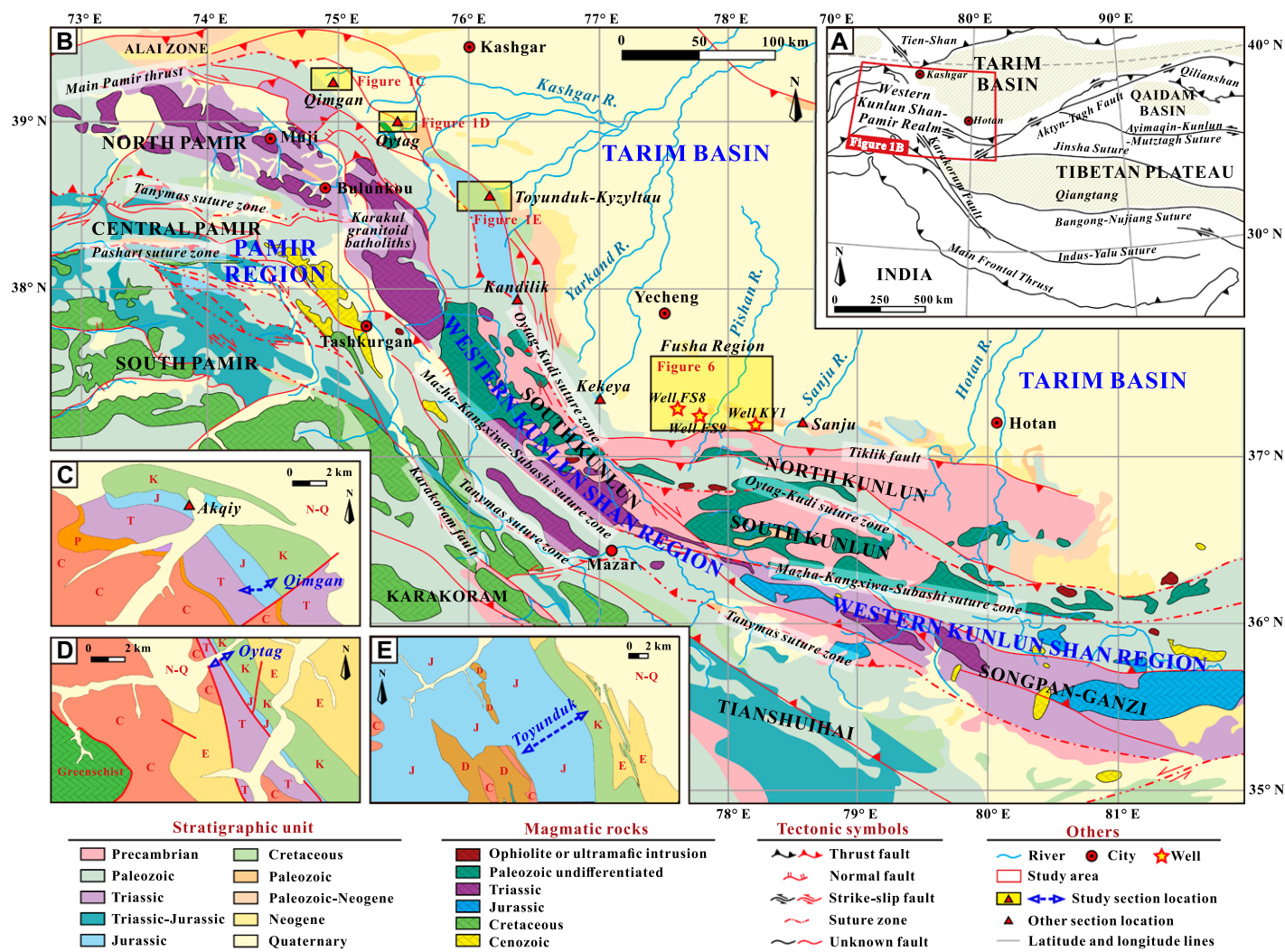Shifa Zhu https://orcid.org/0000-0001-5048-2181
†sfzhu@cup.edu.cn

Figure 1. (A) Regional map of Central Asia, illustrating the Western Kunlun Shan–Pamir Realm in relation to the Tibetan Plateau and India, along with the positions of significant basins, tectonic boundaries, and faults (adapted from Schwab et al., 2004; Robinson et al., 2007; Bershaw et al., 2012). (B) Geologic map of the Western Kunlun Shan–Pamir Realm and Tarim Basin, delineating various tectonic terranes, plutons, clastic deposits, as well as suture zones, modern river systems, and sampling localities (modified from Schwab et al., 2004; Chapman et al., 2018a; Zhang et al., 2019b). The lower left corner features three detailed geological maps centered on the locations of the three sections investigated: (C) Qimgan; (D) Oytag; and (E) Toyunduk-Kyzyltau (modified from Zhang et al., 2019b; Rembe et al., 2022).

challenge lies in securing permissions to conduct research in these areas. As a result, sampling is constrained across the majority of exposed terranes. The sediment factory—that is, the system of bedrock erosion and sediment transport to basins—retains characteristics that enable geologists to decipher information across Earth's surface and interior. Such information includes the nature of the source rocks, tectonic setting, and modes of sediment transport, dispersal, and alteration (e.g., Johnsson, 1993; Weltje and von Eynatten, 2004; von Eynatten and Dunkl, 2012). The southwestern Tarim Basin, bordering the northeastern margin of the Western Kunlun Shan–Pamir Realm, hosts relatively continuous Jurassic sedimentary successions (Sobel,

1999), offering a prime opportunity to examine sedimentary provenance and decode the tectonic evolution associated with the closure of the Western Kunlun Shan–Pamir Paleo-Tethys Realm. Nevertheless, Cenozoic crustal shortening and surface uplift have deformed the Jurassic sediments, restricting our ability to understand the form and origin of Jurassic tectonosedimentary sequences (Schmidt et al., 2011; Sobel et al., 2013), as well as their provenance, and highlighting the need for further investigation.

This study undertakes provenance analysis of Jurassic strata in the southwestern Tarim Basin to explain and discuss the tectonic evolution of the closure of the Western Kunlun Shan–Pamir Paleo-Tethys Realm. To achieve this aim, this

study presents results from a comprehensive investigation that integrates sedimentology (including fieldwork and representative drill cores), thin section observation, heavy mineral signatures, and detrital zircon U-Pb geochronology. The multifold objectives of this work are as follows: (1) to delineate the spatial characteristics of Jurassic provenance differentiation; (2) to establish the tectonic setting of the Jurassic southwestern Tarim Basin and elucidate the interplay between oceanic crust subduction, intracontinental collision, igneous activity, and sedimentary processes; and (3) to develop a refined model for the tectonic evolution of the Western Kunlun Shan–Pamir Paleo-Tethys Realm closure.

This study imposes new constraints on the provenance and tectonic framework of Jurassic sequences, yielding critical insights into the broader geodynamic schema of the Paleo-Tethys Ocean and enriching our knowledge of intracontinental orogenic processes. The findings not only enhance our understanding of the pre-Cenozoic evolutionary processes of the Western Kunlun Shan–Pamir Realm but also of sedimentary basin evolution, crustal evolution, and resource exploration within convergent orogenic settings.

GEOLOGICAL SETTING

Regional Geology

The Western Kunlun Shan Region

The Western Kunlun Shan region forms a natural boundary between the Tarim Basin to the north and the Tibetan Plateau to the south (Fig. 1A), stretching ∼1000 km along the southern margin of Laurasia (Xiao et al., 2003). Tectonically, the Western Kunlun Shan is subdivided into the North Kunlun, South Kunlun, Tianshuihai, and Songpan-Ganzi terranes (Figs. 1B and 2A).

The development of the Western Kunlun Shan region can be broadly categorized into three distinct stages. The first stage, initial construction of the Western Kunlun Shan region, occurred during the early Paleozoic due to the subduction of the Proto-Tethys Ocean (Mattern and Schneider, 2000). The North Kunlun Terrane represents the southernmost uplift of the Tarim Block (Fig. 1B). This Paleozoic oceanic closure led to collision between the Tarim Block and the Tianshuihai Terrane, forming the accretionary South Kunlun Terrane (Xiao et al., 2003). The boundaries between these blocks are the Kudi suture zone to the north of the South Kunlun Terrane (ca. 526–494 Ma; e.g., Li and Zhang, 2014), and the Mazar–Kangxiwa–Subashi suture zone to the south (ca. 487–485 Ma and 455–446 Ma; e.g., Zhang et al., 2021; Zha et al., 2022). Extensive granitoid emplacement occurred in the North Kunlun (ca. 440–410 Ma) and South Kunlun (ca. 510–400 Ma) terranes, reflecting early Paleozoic collisional magmatism (e.g., Zhang et al., 2018; Yin et al., 2020). The closure of the Proto-Tethys Ocean is widely accepted to have occurred between the South Kunlun and North Kunlun terranes at ca. 440–410 Ma (Wu et al., 2020).

The second stage, during the late Paleozoic–early Mesozoic, was a crucial phase in the evolution of the Western Kunlun Shan region, driven by Paleo-Tethys oceanic subduction and the collision between the Cimmerian continent and Tarim Block (e.g., Graham et al., 1993; Matte et al., 1996; Mattern and Schneider, 2000). In the late Paleozoic, the northern periphery of Gondwana experienced the breakup of the continental crust along its margins (Torsvik and Cocks, 2013; Xu et al., 2016). Concurrently, as the Cimmerian continent—including the Songpan-Ganzi and Qiangtang terranes (Fig. 1A)—migrated northward, the Paleo-Tethys Ocean underwent rapid closure (Golonka and Bocharova, 2000). The Mazar–Kangxiwa–Subashi suture zone, south of the South Kunlun Terrane (Fig. 1B), marks the Paleo-Tethys Ocean's final closure (Liu et al., 2020). The collision resulted in the emplacement of extensive granitoids, predominantly arrayed along both flanks of the Mazar–Kangxiwa–Subashi suture zone, with most intrusions dated to the Triassic (e.g., Schwab et al., 2004).

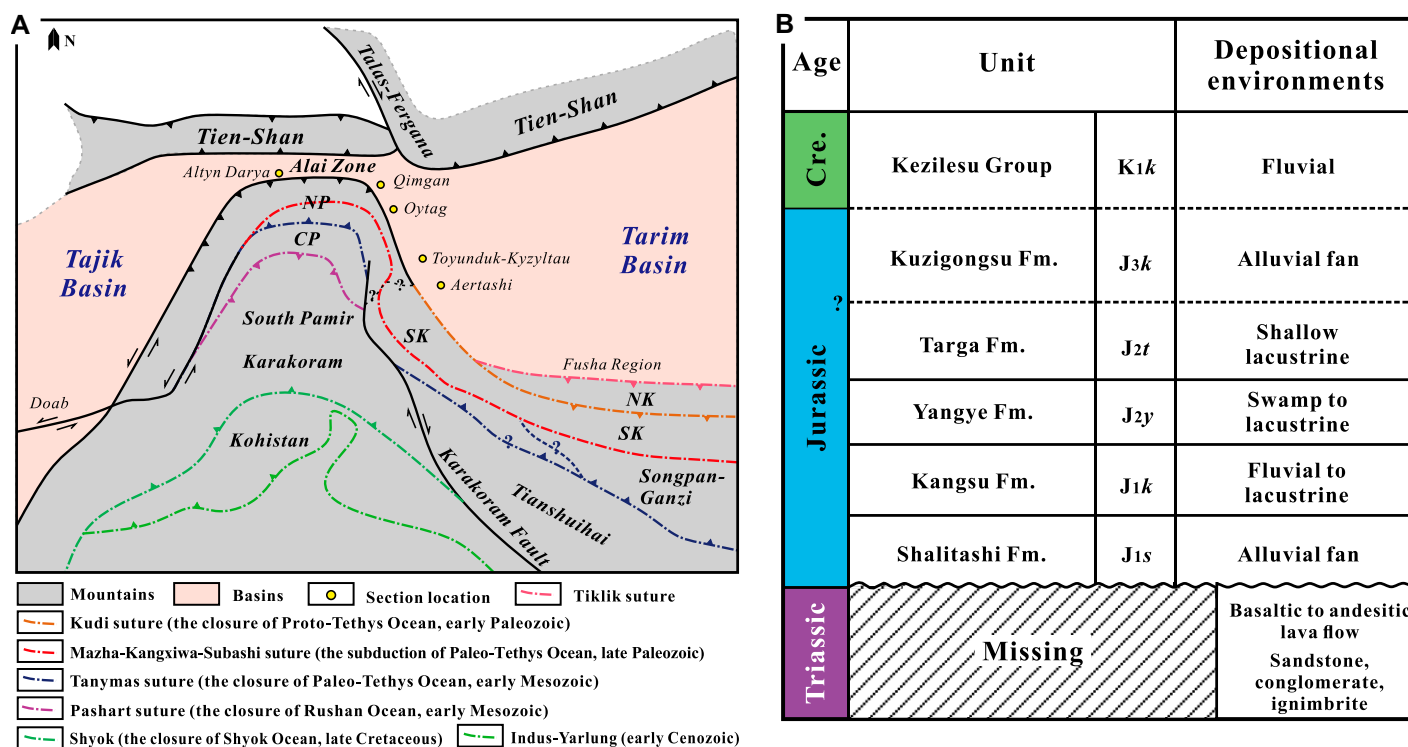| Age	Unit		Depositional environments
Cre.	Kezilesu Group	K_1k	Fluvial
Jurassic	Kuzigongsu Fm.	J_3k	Alluvial fan
Jurassic	Targa Fm.	J_2t	Shallow lacustrine
Jurassic	Yangye Fm.	J_2y	Swamp to lacustrine
Jurassic	Kangsu Fm.	J_1k	Fluvial to lacustrine
Jurassic	Shalitashi Fm.	J_1s	Alluvial fan
Triassic	Missing		Basaltic to andesitic lava flow; Sandstone, conglomerate, ignimbrite

Figure 2. (A) The present tectonic framework of the Western Kunlun–Pamir Paleo-Tethys Realm with the prominent suture zones (adapted from Zanchetta et al., 2018). (B) Stratigraphic classification and the associated depositional environments of Jurassic strata within the southwestern Tarim Basin, as delineated by Sobel (1999) and Rembe et al. (2022). The Triassic strata are largely absent; they can be observed only in a few sections. A parallel unconformable contact is observed within the J_2t–J_3k strata and the overlying Jurassic and Cretaceous (Cre.) strata. SK—South Kunlun Terrane; NK—North Kunlun Terrane; J_1s—Shalitashi Formation; J_1k—Kangsu Formation; J_2y—Yangye Formation; J_2t—Targa Formation; J_3k—Kuzigongsu Formation; K_1k—Kezilesu Group.

Geological Society of America Bulletin

The third stage occurred throughout the Mesozoic. The Western Kunlun Shan region remained in a state of continuous uplift at that time. Closure of the Neo-Tethys Ocean and the Indian-Eurasian collision (e.g., Hendrix et al., 1992; Cao et al., 2015) drove significant reactivation and uplift in the late Mesozoic and Cenozoic.

The North Kunlun and South Kunlun terranes are predominantly characterized by Precambrian metamorphic complexes, volcano-sedimentary successions, and unmetamorphosed carbonate–clastic sequences (Fig. 1B; Zhang et al., 2019a). Abundant Paleozoic and Triassic granitoids are distributed along northwest–southeast-trending faults (Fig. 1B; e.g., Yuan et al., 2002; Wang et al., 2017; Yin et al., 2020). The Tianshuihai Terrane is primarily composed of Paleozoic and Mesozoic (metamorphosed) sedimentary rocks (e.g., Matte et al., 1996; Cowgill et al., 2003; Luo et al., 2024). The Songpan-Ganzi Terrane mainly consists of Triassic and Jurassic plutons and also contains Triassic sedimentary rocks (e.g., Yin and Harrison, 2000; Xiao et al., 2007; Ding et al., 2013). The boundary between the Tianshuihai and Songpan-Ganzi terranes is commonly established along the Tanymas suture (Fig. 1B and 2A). However, the details remain controversial.

The Pamir Region

Geographically, the Pamir region adjoins the Alai Zone to the north and separates the Tarim and Tajik basins to the east and west, respectively (Fig. 2A). Pamir is internally divisible into three principal terranes: the North Pamir, Central Pamir, and South Pamir, which are demarcated by the Tanymas and Pashart suture zones, respectively (Fig. 1B; Schwab et al., 2004; Robinson, 2015; Song et al., 2024).

The North Pamir Terrane represented the southern margin of Asia during the late Paleozoic to early Mesozoic (Aminov et al., 2023). The subduction of the Paleo-Tethys Ocean gave rise to extensive Carboniferous–Permian, arc-like volcanic eruptions (Bazhenov, 1996; Song et al., 2024) composed of basalt, dacite, and volcanic breccia (Song et al., 2024). These volcanic rock assemblages are well exposed, accessible, and have been carefully dated in the Oytag region (Fig. 1B), which is bordered to the south by the Triassic Karakul granitoid batholiths (Rembe et al., 2022). Subsequently, the amalgamation of the North Pamir, Central Pamir, and South Pamir terranes occurred, leading to the formation of extensive Triassic collisional granitoid batholiths (Karakul-Mazar) within the North Pamir Terrane. Thus, the North Pamir Terrane is predominantly composed of Paleozoic and Triassic sedimentary rocks, along with Carboniferous–Permian volcanic rock assemblages and numerous Mesozoic granitoids (Fig. 1B; Schmidt et al., 2011; Blayney et al., 2016). Previous consensus suggested the Pamir domain migrated significantly due to Cenozoic northward indentation of the North Pamir Terrane (e.g., Burtman and Molnar, 1993; Cowgill, 2009). However, newer evidence points to a less extensive displacement (e.g., Chapman et al., 2017; Li et al., 2019b), with the Pamir salient's curvature likely due to plate boundary geometry rather than internal deformation (Li et al., 2020).

The convergence and eventual closure of the Paleo-Tethys Ocean between the North Pamir and Central Pamir terranes occurred in the Late Triassic, coinciding with the concomitant closure of the Rushan Ocean between the Central Pamir and South Pamir terranes. This activity formed two suture zones: the Tanymas and the Pashart (Fig. 1B and 2A; Robinson, 2015). During the Cretaceous, the emplacement of extensive granitoid intrusions within the South Pamir and Karakoram terranes (ca. 130–95 Ma) marked the closure of the Shyok Ocean (Fig. 2A; e.g., Faisal et al., 2016; Aminov et al., 2017; Chapman et al., 2018b). The Central Pamir Terrane is characterized by a predominance of Paleozoic and Triassic–Jurassic clastic and carbonate successions, as well as Cenozoic orthogneiss (Fig. 1B; Schmidt et al., 2011; Hacker et al., 2017). Similarly, the South Pamir Terrane is primarily composed of Paleozoic strata, Triassic–Jurassic strata, and extensive Cretaceous and Cenozoic magmatic rocks (e.g., Schwab et al., 2004; Robinson, 2015; Blayney et al., 2016).

Jurassic Stratigraphic System in the Southwestern Tarim Basin

The Tarim Basin constitutes a vast Mesozoic–Cenozoic intracontinental composite basin, superimposed upon a Paleozoic platform and Proterozoic metamorphic crystalline basement (Tian et al., 1989). It is positioned to the south of the Tien-Shan Mountains, north of the Western Kunlun Shan region, and is overthrust by the Pamir region to the west (Fig. 1A).

The study area is located in the southwestern Tarim Basin. Sobel (1999) and Wu et al. (2021, 2025) analyzed and documented the Triassic–Jurassic basin of this region. Therefore, only a concise review is presented here. The Triassic tectonic setting is characterized by regional compression. A deformation belt, ∼60 km in width, characterized by fold-and-thrust structures, was established along the southwestern margin of the Tarim Basin, which was precipitated by the collision of the Qiangtang Terrane with Eurasia (Fig. 1A). This collision led to substantial topographic uplift. As a result, there are few substantially preserved accumulations of Triassic strata in the southwestern Tarim Basin. Recent research has identified Triassic basaltic to andesitic lavas and associated volcaniclastic strata exclusively within a few select sections, notably the Qimgan and Oytag sections (Figs. 1C and 1D; Rembe et al., 2022). The Jurassic witnessed the formation of several narrow, deep, and discrete extensional grabens in the southwestern Tarim Basin, stretching along the Western Kunlun Shan–Pamir Realm, whereas the overlying Jurassic strata were sequentially deposited on either the sparsely preserved Triassic strata or the folded Paleozoic sequences. During the Jurassic, alluvial fan and intermontane river systems originating from the Western Kunlun Shan–Pamir Realm constituted the primary pathways for sediment supply, with ultimate deposition in a series of alluvial and lacustrine settings (Fig. 2B). The Jurassic sedimentation was predominantly governed by fault dynamics, which influenced the locations and timing of sediment accumulation and the resultant stratal thickness variations.

Previous Provenance Studies of Jurassic Sedimentary Records

Sobel (1999) proposed that the depocenters of the Jurassic basins trended generally northnorthwest, subparallel to the axis of the Western Kunlun Shan–Pamir Realm. The eastern flank of the Pamir region and the westernmost portion of the Kunlun region served as the principal elevated source area for Jurassic sediments. Bershaw et al. (2012) conducted detrital zircon analysis on one J_1s (Shalitashi Formation)–J_2t (Targa Formation) clastic rock sample from the Oytag section (Fig. 1D), revealing that the deposits were predominantly derived from Triassic igneous rocks. Zhang et al. (2019b) further supplemented detrital zircon analysis with one Jurassic J_3k (Kuzigongsu Formation) sandstone sample from the Toyunduk-Kyzyltau section (Fig. 1E). They posited that a westward-draining pattern, evolved by headward erosion, was established during the Jurassic across the Western Kunlun Shan region and North Pamir Terrane, with no significant contribution of detrital sediments from the Central Pamir and South Pamir terranes. Subsequently, Wu et al. (2025) undertook comprehensive field investigations of Jurassic strata in the Toyunduk-Kyzyltau and Kandilik sections (Fig. 1B). They conducted detrital zircon analysis of three samples from the J_1s–J_2t strata, and posited that there may be areas where the J_1s–J_2t strata are in parallel unconformable contact with the Jurassic J_3k strata, potentially altering the dynamics of the source-to-sink system.

METHODOLOGY

Sampling

In this study, our work focused on examination of three outcrops (Qimgan, Oytag, and Toyunduk-Kyzyltau) and three wells (FS8, FS9, and KY1) in the southwestern Tarim Basin. We collected 138 samples (Table S1 in the Supplemental Material[1]) from sites selected to encompass the primary catchments that drained the surrounding mountains during the Jurassic (Fig. 1B). Sedimentological data, including composition, grain size, sedimentary structures, bedding geometry, and color, were recorded to delineate stratigraphic boundaries and define sedimentary facies (Table S4). Subsequently, petrological and detrital zircon U-Pb analyses were conducted on 82 sandstone and conglomerate samples from J_1s–J_2t strata to differentiate Jurassic provenance. This research approach can mitigate the potential influence of provenance variations that may arise at the internal unconformable boundaries within the Jurassic (between the J_2t and J_3k strata; Wu et al., 2025), thereby improving the reliability of the results. Furthermore, the sandstones and conglomerates at the base of the Jurassic preserve more comprehensive information about the tectonic evolution of the orogenic belt than those in the upper portion.

We collected previously published U-Pb data on detrital zircons from modern river sands to delineate the geochronological signature of the source area (Lukens et al., 2012; Carrapa et al., 2014; Blayney et al., 2016; Rittner et al., 2016; Liu et al., 2017). Using modern river sands for terrane characterization is preferable to using bedrock samples because river sands provide a more representative average of a broader area (e.g., Blayney et al., 2016). It is crucial to emphasize that despite the utility of modern river sand samples for characterizing source area signals, significant biases are introduced due to factors such as the variable fertility of zircons, the sand-generation potential of various lithologies, the distances of transport, and the processes of recy-

cling (Castillo et al., 2022). These elements can lead to the data being nonquantitatively representative across all scales. Therefore, this study used the observed distribution of U-Pb detrital zircon ages from modern rivers as a qualitative proxy for potential source regions, not as a precise quantitative measure.

Thin-Section Observation

Thin sections of 54 J_1s–J_2t samples were prepared to identify the detrital components within sandstones. Each thin section was impregnated with blue-dyed epoxy and stained with alizarin red-S solution to improve the visibility and recognition of carbonate minerals. A point-counting procedure based on the Gazzi-Dickinson method was used to analyze the framework composition of sandstone samples. For each thin section, >300 points were counted. Only grains >62.5 μm were included in the count. In addition, we also recorded the proportions of matrix, cement, and visible pore when the microscope crosshair landed on areas outside of the grains. This expanded point-counting approach allows not only provenance interpretation through quartz-feldspar-lithic fragment (Q-F-L) data, but also permits insights to be made regarding the diagenetic history of the sandstones. Grain size estimation in thin sections was conducted using a visual comparison method based on modal grain size ranges. Although semiquantitative, this approach has been widely applied in petrographic studies due to its efficiency and reasonable accuracy (e.g., Li et al., 2017). We used the standard scheme proposed by Folk (1980) to classify sandstone grain sizes. An Olympus BX51 metallographic microscope was used for observation, with both plane-polarized and cross-polarized light, and the Olympus Stream imaging system (Olympus Soft Imaging Solutions GmbH) was also employed. Table S2 provides detailed sample information and data. Our study plotted the statistical petrographic data in Q-F-L and volcanic-metamorphic-sedimentary (Lv-Lm-Ls) diagrams (Garzanti, 2019) for petrographic classification.

Heavy Mineral Analysis

Heavy mineral analysis was performed on 18 J_1s–J_2t sandstone samples from outcrops characterized by alluvial-fan or river-delta facies. Approximately 20 g of each sample was subjected to a series of treatments, including soaking in a 10% hydrochloric acid solution, grinding, panning with water, and drying. Following this process, particles ranging from 63 μm to 250 μm were selected as subsamples (~5 g). To separate the heavy mineral fraction, these

subsamples were treated with a tribromomethane solution with a density of 2.86 g/cm³. The separated heavy minerals were then mounted on 2-mm-thick glass slides with epoxy resin and identified using a Zeiss petrographic microscope (Axio Imager A1). Minerals of possible authigenic origin, such as siderite and anhydrite, were also counted but were excluded from the detrital assemblage. We normalized the raw counts of the remaining heavy mineral phases to 100% to compare the Jurassic provenance characteristics between different sections and wells.

In this study, we also employed the provenance-sensitive parameters Garnet Zircon Index (GZI) and Zircon-Tourmaline-Rutile Maturity Index (ZTR) for comparative analysis of distinct source origins. The GZI is calculated as GZI = 100% × garnet/(garnet + zircon) (Morton and Hallsworth, 1994). The ZTR represents the cumulative percentage of ultrastable minerals, which includes zircon, tourmaline, and all phases of TiO_2 (Hubert, 1962). These parameters were computed and subsequently plotted to further evaluate the degree of scatter within the dataset.

Detrital Zircon U-Pb Geochronology

A total of 10 J_1s–J_2t rock samples (weighing ~2 kg each) were disaggregated using an electric pulse disaggregation apparatus. The separation of detrital zircon fractions was accomplished by magnetic and heavy liquid separation techniques. A total of 250 zircons with diverse sizes and crystal habits were manually selected from each sample. The zircons were mounted in 25-mm epoxy discs and polished with 7000 mesh silicon carbide paper and 0.05-μm-diameter aluminum oxide to reveal the cores of the grains. Each mount was imaged using cathodoluminescence (CL) to capture its internal textures. CL imaging was conducted with a TESCAN MIRA3 scanning electron microscope operating at an accelerating voltage of 7 kV, with an exposure time set to 2 min for clear image acquisition. Zircon grains with intact surfaces, varying size and shape, and an absence of fluid inclusions were selected for analytical spot localization. Final analytical targets consisted of 120 spots for each outcrop sample and 110 spots for each drilling sample.

For laser ablation–inductively coupled plasma–mass spectrometry (LA-ICP-MS) analysis, zircon U-Pb dating was conducted at the Beijing Quick-Thermo Science and Technology Co., Ltd., utilizing an ESI New Wave NWR 193UC (TwoVol2) laser ablation system coupled with an Agilent 8900 triple quadrupole ICP-MS. The laser parameters were set to a spot size of 20 μm and a frequency of 5 Hz. Zircon standard

---

[1]Supplemental Material. Table S1: Detailed sample collection information and section locations. Table S2: Petrographic summary of Jurassic sandstones from the southwestern Tarim Basin. Table S3: Full zircon U-Pb dataset for Jurassic samples from the southwestern Tarim Basin. Table S4: Sedimentological characteristics and environmental interpretation of Jurassic strata in the southwestern Tarim Basin. Table S5: Pollen statistics table from the Jurassic Aketao section in the southwestern Tarim Basin. Please visit https://doi.org/10.1130/GSAB .S.29944211 to access the supplemental material; contact editing@geosociety.org with any questions.

91500 was employed as the primary reference material for all U-Pb age determinations, with Plešovice zircon serving as the secondary reference (Sláma et al., 2008). Background subtraction and correction for laser-induced elemental fractionation were applied using the Iolite data reduction package within the Wavemetrics Igor Pro data analysis software (Paton et al., 2010). Detailed instrument conditions and experimental procedures are described by Ji et al. (2020), and Table S3 also provides a full description of the method. Probability density plots and peak ages were generated with Isoplot 4.15. The ^{206}Pb/^{238}U ratio was used for age determination of grains younger than 1000 Ma, while the ^{207}Pb/^{206}Pb ratio was used for older grains. Data filtering was performed using standard discordance tests with a 10% threshold.

Multidimensional scaling (MDS) is a powerful technique for dimensionality reduction. It is widely applied in provenance analysis and the data mining of detrital zircon age datasets (Vermeesch, 2013; Stevens et al., 2013). The 3-D MDS plot generated by DZstats 2.30 (Saylor and Sundell, 2016) facilitates the clustering of Jurassic samples that share similar age spectra, while simultaneously differentiating those with distinct spectral characteristics. In this study, we employed a matrix of pairwise Euclidean distances to graphically represent and quantify the degree of similarity between each sample (Vermeesch, 2013).

STRATIGRAPHY AND PETROGRAPHY

Here, we present the stratigraphic and petrographic details of the three outcrops and three wells investigated. The stratigraphic columns succinctly depict the principal stratigraphic attributes of different formations. Table S4 collates the sedimentological attributes of each section and offers a concise interpretation of the depositional environments.

Qimgan Section

Field Observations

The Jurassic strata in the Qimgan section are characterized by the continuous and excellent exposure of conglomerate, gravelly sandstone, and sandstone, intercalated with a minor occurrence of thin, coal-bearing mudstone layers (see Table S4 for detailed explanations), with a total thickness of ~1950 m (Fig. 3A). The earthy yellow and dark green andesitic conglomerate of the Triassic abruptly transitions upward into the purple-brown alluvial conglomerate of the J_1s, with a clear angular unconformity detected in the field. Conformable contact relationships are observed between the stratal units within the J_1s–J_2t system, whereas a parallel unconformable contact relationship is noted within the J_2t–J_3k system and the Jurassic and overlying Cretaceous strata (Fig. 3J).

Petrography

The sandstones we examined exhibit considerable complexity, but overall, they mainly plot within the fQL field in the Q-F-L diagrams (Fig. 4A). The framework component is $Q_{34.0}F_{20.6}L_{45.4}$, with an average matrix content of 7.1%. Quartz grains comprise 34.0% of the total framework grains, and are characterized by water-clear appearances, smooth surfaces, and sharp angular habits (Fig. 3F). Feldspars, including plagioclase and sanidine, are common and sometimes relatively abundant, but microcline is almost absent. The presence of oscillatory zoning and corroded embayment in plagioclase is commonly observed (Fig. 3G). Lithics constitute an average of ~45% and are primarily composed of mafic–intermediate volcanic rocks (Fig. 3H), with some granitoid (Fig. 3I) and rhyolitic lithics present. All of the samples plot closer to the Lv pole in the Lv-Lm-Ls diagrams, with an average composition of $Lv_{80.8}Lm_{9.3}Ls_{9.9}$ (Fig. 4A).

The sandstones, regardless of grain size, had similar framework components and lithic compositions. Labile clastic grains (e.g., plagioclase and basaltic lithics) preserve their original structural integrity and only exhibit slight compaction-induced deformation (Fig. 3H). Examination of the thin sections reveals few dissolution features, with the majority displaying slight or no signs of cementation (Figs. 3F–3I).

Oytag Section

Field Observations

Comparable to the Qimgan section, the Oytag section exhibits a similar Jurassic stratigraphy, predominantly composed of a well-preserved sequence of conglomerate and sandstone that is occasionally interrupted by discrete layers of thin, coal-bearing mudstones (Fig. 5A). Although the exposed thickness of the Jurassic strata is only ~460 m, the stratigraphic sequence is intact. The Jurassic strata initiate with the J_1s layer, characterized by earthy yellow conglomerate in faulted contact with underlying Triassic basalt (Fig. 5B). The section transitions upward into earthy yellow and dark gray gravelly sandstone, interlayered with carbonaceous mudstone and thin coal seams in the J_1k (Kangsu Formation) and J_2y (Yangye Formation) strata. The uppermost Jurassic strata consist of clast-supported conglomerate interbedded with dull red and grayish-green mudstone.

Petrography

The sandstones analyzed in the Oytag section collectively occupy a transitional zone situated at the boundaries of five distinct fields (Fig. 4B). However, in a stricter sense, the medium-grained sandstones predominantly fall within the LQ field, whereas the coarse-grained sandstones are more likely to be assigned to the fQL field, although the overall difference is small (Fig. 4B). The framework component is $Q_{47.9}F_{12.0}L_{40.1}$, with an average matrix content of 2.9%. The samples also collectively exhibit a pronounced tendency to cluster near the Lv pole in the Lv-Lm-Ls diagrams, with an average composition of $Lv_{76.2}Lm_{13.0}Ls_{10.8}$ (Fig. 4B). The crystallographic and diagenetic characteristics of the various clastic grains exhibit a high degree of similarity to those of the Qimgan sandstones. Thus, they are not described again here.

Toyunduk-Kyzyltau Section

Field Observations

The base of the Jurassic strata was inaccessible, leaving the underlying stratigraphic contact relationship undetermined for this section.

Figure 3. (A) Composite stratigraphic section of the Jurassic strata at the Qimgan section. See Figure 1B for the location of the Qimgan section. Approximate stratigraphic positions of the zircon U-Pb samples (stars), thin section samples (triangles), and heavy mineral samples (squares) are indicated. **(B)** Longitudinal profile exhibiting couplets of structureless, coarse-grained cobble and indistinct cross-bedding fine-cobble and/or coarse-pebble conglomerates. **(C)** Parallel-bedded, pebbly sandstone and coal-bearing mudstone interpreted as braided river and floodplain deposits. **(D)** Parallel-bedded, coarse- to medium-grained sandstone and coarse-pebble conglomerate. **(E)** Light gray siltstone and purple-brown siltstone, interpreted as delta front or shallow-lacustrine deposits. **(F)** Coarse-grained, high-temperature quartz (Q) from sample QM-10, taken in cross-polarized light (XPL). **(G)** Oscillatory zoning and corroded embayments of plagioclase from sample QM-6, XPL. **(H)** Mafic volcanic lithic (VL) from sample QM-1, taken in plane-polarized light (PPL). **(I)** Granitoid lithics from sample QM-1, XPL. **(J)** Parallel unconformity between the J_2t, J_3k, and Cretaceous strata at the Qimgan section. F—feldspar; PL—plutonic lithics. Color-coding corresponds to the lithological types depicted in the vertical section.
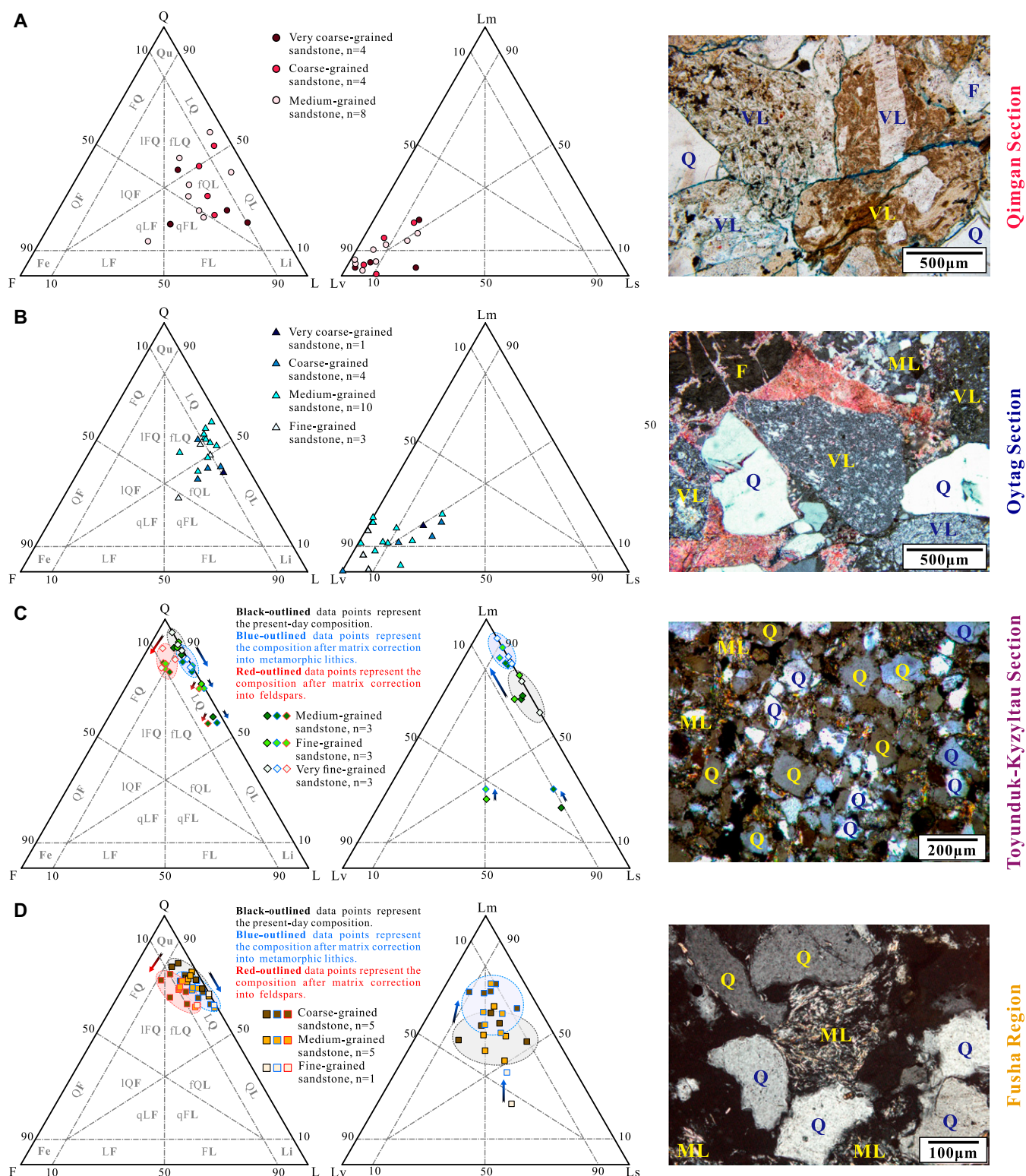
Geological Society of America Bulletin
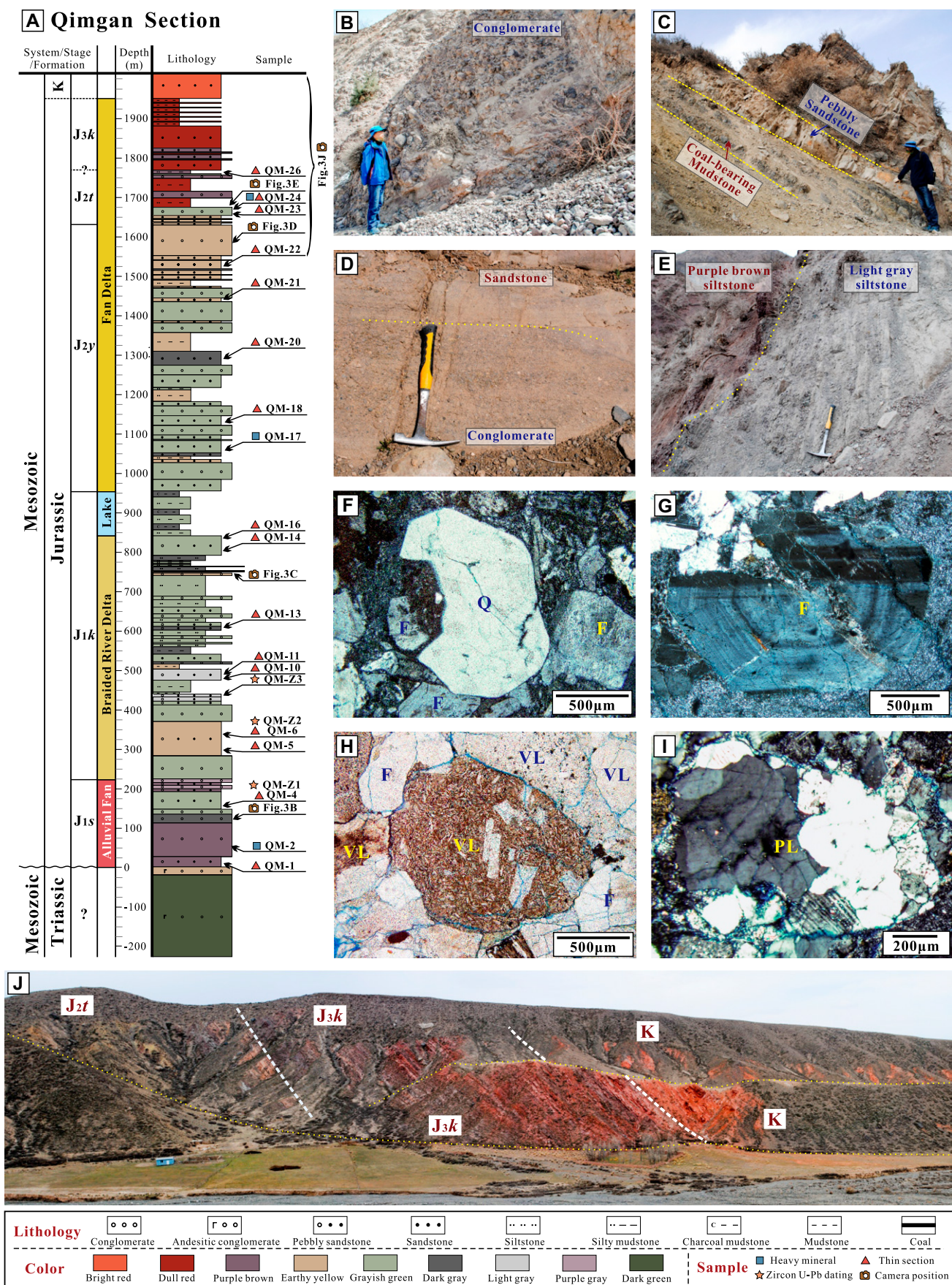
Figure 4. Point-counting results are presented in the quartz-feldspar-lithic fragment (Q-F-L) and volcanic lithics–metamorphic lithics–sedimentary lithics (Lv-Lm-Ls) triangular diagrams, as proposed by Garzanti (2019), alongside representative microscopic images of various sections and wells. (A) Qimgan section; (B) Oytag section; (C) Toyunduk-Kyzyltau section; (D) Fusha region. F—feldspar; Fe—feldspathic; FL—feldspatho-lithic; fLQ—feldspatho-litho-quartzose; FQ—feldspatho-quartzose; fQL—feldspatho-quartzo-lithic; LF—litho-feldspathic; lFQ—litho-feldspatho-quartzose; Li—lithic; LQ—litho-quartzose; lQF—litho-quartzo-feldspathic; ML—metamorphic lithics; Q—quartz; QF—quartzo-feldspathic; qFL—quartzo-feldspatho-lithic; QL—quartzolithic; qLF—quartzo-lithofeldspathic; Qu—quartzose; VL—volcanic lithics.
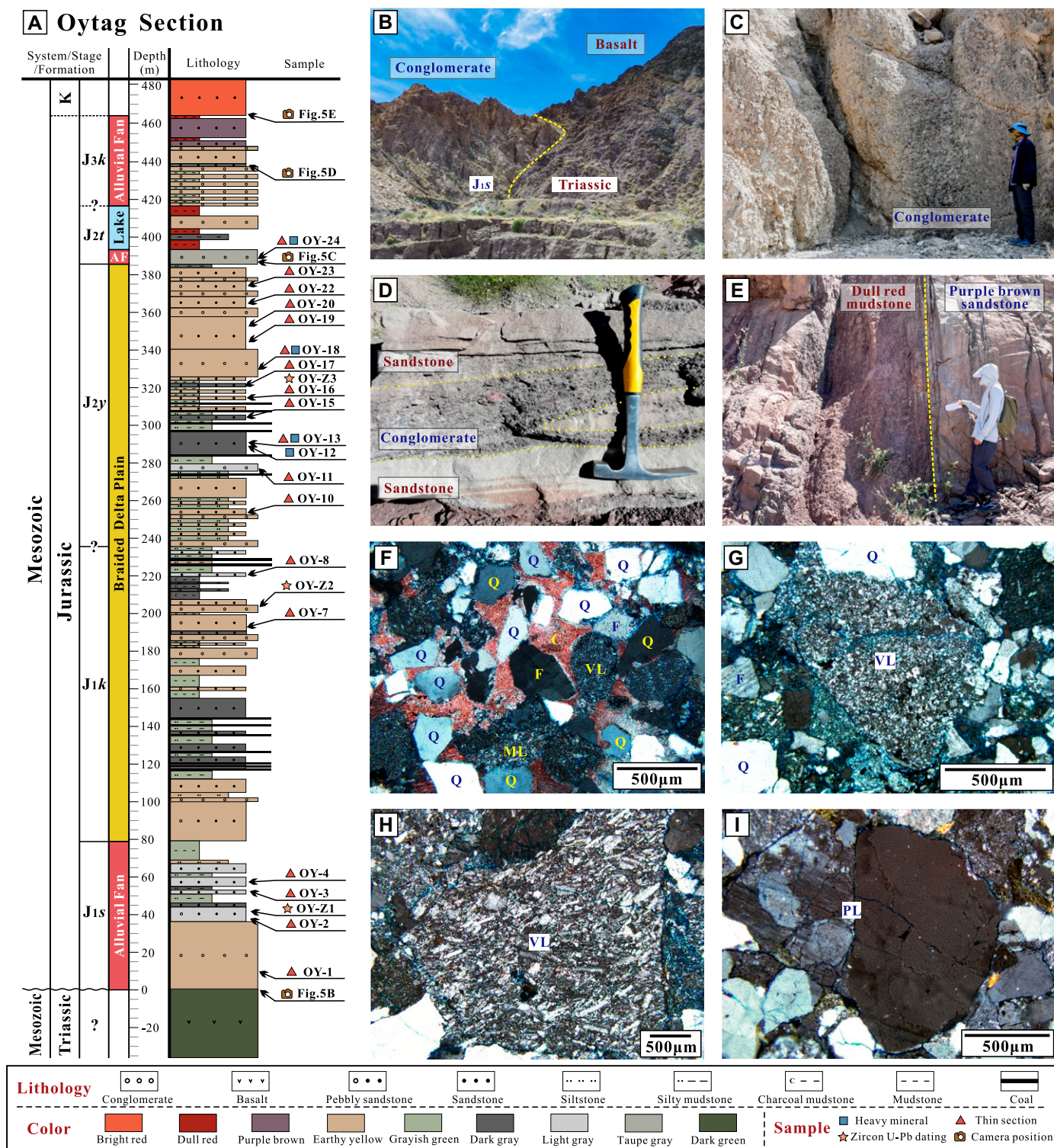
Figure 5. (A) Composite stratigraphic section of the Jurassic strata at the Oytag section. See Figure 1B for the location of the Oytag section. **(B)** Angular unconformity that separates the Jurassic conglomerate from the underlying Triassic basalt. **(C)** Planar-interstratified coarse- and/or fine-pebble conglomerate interpreted as alluvial fan deposits. **(D)** Interbedded coarse-grained sandstone and fine conglomerate with cross-bedding, interpreted as channel deposits of alluvial fan. **(E)** The thick sequence of dull red mudstone and purple-brown sandstone at the top of the Jurassic strata. **(F)** Monocrystalline quartz grains characterized by a water-clear appearance, smooth surfaces, and a sharply angular habit from sample OY-3, taken in cross-polarized light (XPL). **(G)** Intermediate–felsic volcanic lithic from sample OY-19, XPL. **(H)** Mafic–intermediate volcanic lithic from sample OY-23, XPL. **(I)** Granitoid lithic from sample OY-11, XPL. AF—alluvial fan; C—calcite cements; F—feldspar; PL—plutonic lithics; ML—metamorphic lithics; Q—quartz; VL—volcanic lithics.

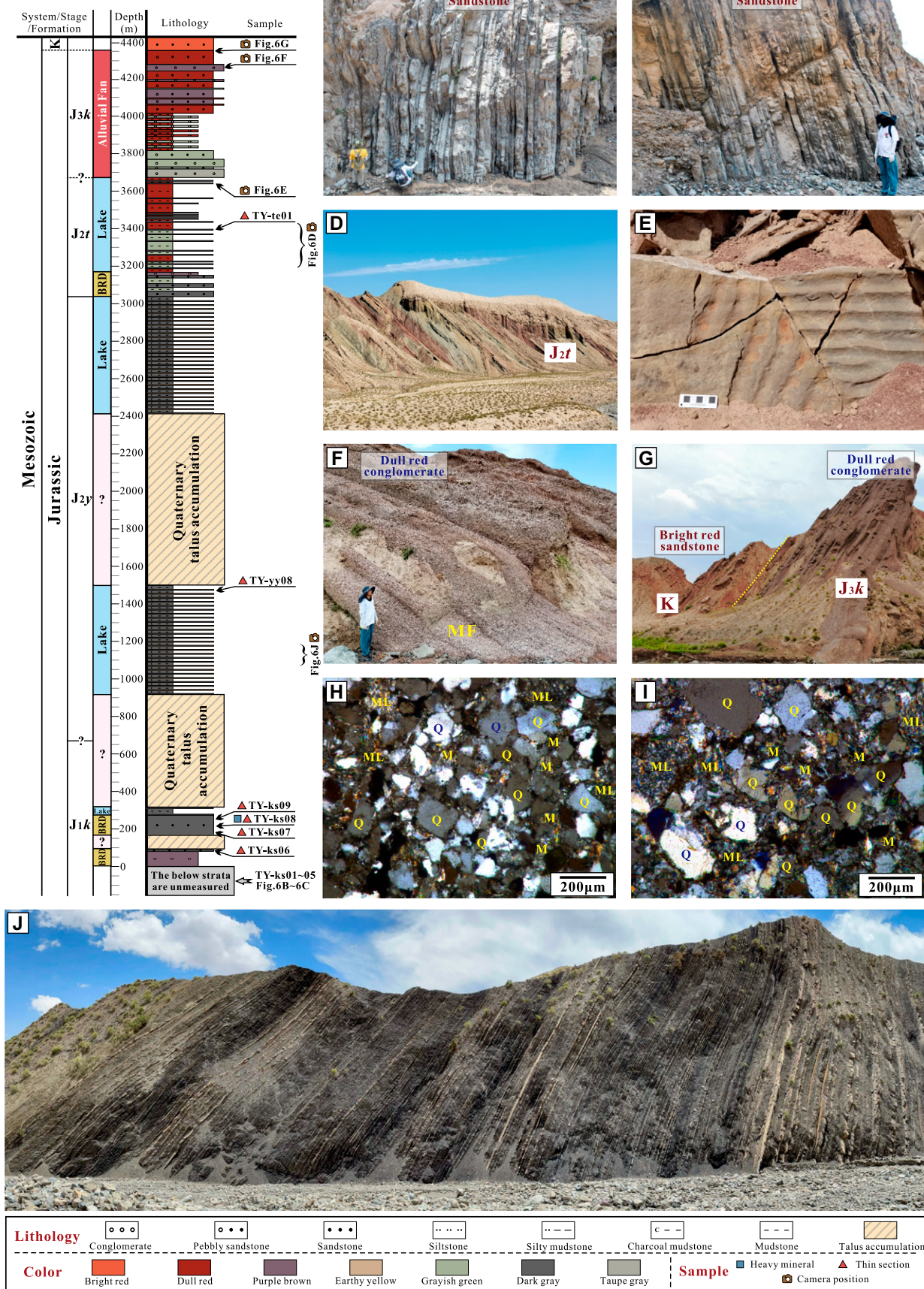**A** Toyunduk–Kyzyltau Section

Figure 6. (A) Composite stratigraphic section of the Jurassic strata from the Toyunduk-Kyzyltau section. See Figure 1B for the location of the Toyunduk-Kyzyltau section. (B) Interbedded sandstone and siltstone, interpreted as channel deposits of braided-delta-plain deposits. (C) Interbedded massive sandstone and laminated siltstone, interpreted as channel deposits of braided-delta-plain deposits. (D) Alternating layers of fine-grained clastic rock series in the J_2t strata of the Toyunduk-Kyzyltau section. (E) Ripples on the surface of sandstone. (F) Sequence of dull red conglomerate at the top of the Jurassic strata, interpreted as alluvial fan deposits. (G) Parallel unconformity between the Jurassic and Cretaceous at the Toyunduk-Kyzyltau section. (H) Quartz grains and metamorphic lithics with cloudy and rough surfaces from sample TY-ks09, taken in cross-polarized light (XPL). (I) Quartz grains and metamorphic lithics with cloudy and rough surfaces from sample TY-ks07, XPL. (J) Frequent interbedding between coal seams and siltstones, hundreds of meters in thickness. BRD—braided river delta; M—matrix; ML—metamorphic lithics; Q—quartz.

Regional geological mapping suggests that the Jurassic unconformably overlies Carboniferous strata (Fig. 1E). The Toyunduk-Kyzyltau sequence begins with the J_1k strata, primarily consisting of taupe-gray sandstone interlayered with carbonaceous mudstones and thin coal seams (Fig. 6A). The J_2y strata are characterized by the frequent interlayering of earthy-yellow rippled or horizontally burrowed siltstone and dark gray to black shale. The shale contains disseminated leaf fragments and thin coal beds (laterally continuous for thousands of meters, though part of the strata is obscured by Quaternary talus). The uppermost Jurassic strata predominantly feature laterally continuous dull red to grayish-green siltstone interbedded with fine-grained sandstones and plant fossils, deposited throughout the J_2t strata, as well as dull red to purple-brown massive conglomerate, deposited in the J_3k strata. The measured thickness of the Jurassic strata is ~4400 m.

Petrography

The sandstones we studied in the Toyunduk-Kyzyltau section are predominantly categorized as quartzose and lithoquartzose (Fig. 4C), exhibiting an average composition of $Q_{84.3}F_{0.9}L_{14.8}$, with an average matrix content of 6.5%. The Toyunduk-Kyzyltau sandstones are distinguished by abundant quartz grains and exceptionally low content of feldspar grains. The quartz grains consist primarily of monocrystalline grains (averaging ~72%) and polycrystalline grains (averaging ~13%), typically exhibiting a subrounded morphology with moderate sorting (Fig. 6H). The occurrence of cloudy and rough surfaces on individual quartz grains is commonly observed. Lithics are predominantly composed of metamorphic (phyllite and schist; Fig. 6I) and sedimentary lithics (siltstone). Metamorphic lithics collectively predominate over sedimentary lithics, and the proportion of volcanic lithics is significantly less than in the Qimgan and Oytag sections (Fig. 4C). The average lithic composition is $Lv_{6.7}Lm_{61.6}Ls_{31.7}$. Variations in grain size did not significantly affect the framework or lithic composition.

Notably, the Toyunduk-Kyzyltau samples exhibit certain alteration of labile grains, par-

ticularly feldspars. Under compaction, some lithics and altered feldspars underwent plastic deformation and were squeezed into intergranular spaces, forming pseudomatrices (Figs. 6H and 6I; Galloway, 1974). The matrix is characterized by weakly aligned sericite flakes and silt-sized quartz and feldspars, with features indicative of either a metamorphic origin (from schist or phyllite lithics) or alteration of feldspar along cleavage planes. Given the inherent difficulty in reliably distinguishing protomatrix from pseudomatrix, a conservative approach was adopted in which all matrix material was provisionally reassigned to either the metamorphic lithic or feldspar components. This approach yielded a maximum estimate of (metamorphic) lithic and feldspar content, whereas the uncorrected values represent the minimum. Accordingly, the actual composition is expected to lie between these three parts, providing a more constrained basis for provenance and compositional interpretation (Fig. 4C). After matrix correction, the average framework components are $Q_{78.4}F_{0.9}L_{20.7}$ (assigned to metamorphic lithics) and $Q_{78.4}F_{7.6}L_{14.0}$ (assigned to feldspars), with the lithic composition comprising $Lv_{5.7}Lm_{73.2}Ls_{21.1}$ (assigned to metamorphic lithics).

Fusha Region (Wells FS8, FS9, and KY1)

Observations

In Well FS8, the Jurassic strata are ~1700 m thick (Fig. 7A). The basal Jurassic is comprised of conglomerate and sandstone interbedded with siltstone, with a thickness of ~300 m (all sampling and analysis in this well were focused in this interval). Upsection, the strata transition into gray to black mudstone, with a few relatively thin intercalations of siltstone, sandstone, coal seams, and plant fossils, reaching a thickness of ~1400 m. The Jurassic strata in Well FS9 are ~1700 m thick and have stratigraphic contact relationships and lithologic characteristics similar to those of Well FS8 (Fig. 7B). The notable difference is that the basal, coarse-grained deposits in Well FS9 are only ~30 m thick. In Well KY1, the Jurassic strata are ~200 m thick (Fig. 7C). The lower half is predominantly conglomerate with a few relatively thin intercala-

tions of finer-grained sediments. As the proportion of gravel decreases toward the upper half, there is a significant phase of coal seam deposition, accompanied by the continuous deposition of sandstone and conglomerate.

Petrography

All samples in the Fusha region plot within the LQ fields (Fig. 4D), with a mean framework component of $Q_{74.1}F_{3.5}L_{22.4}$. The average matrix content is 6.1%. The quartz grains consist of monocrystalline grains (averaging ~61%) and polycrystalline grains (averaging ~14%). The lithics are predominantly metamorphic (Figs. 7E–7G). The volcanic lithic content, which averages ~5%, is notably lower than in the Qimgan and Oytag sections. All samples plot closer to the Lm pole in the Lv-Lm-Ls diagrams (Fig. 4D), with an average composition of $Lv_{21.6}Lm_{50.2}Ls_{28.2}$. The crystallographic and diagenetic characteristics of the various clastic components and matrices exhibit a high degree of similarity to those of the Toyunduk-Kyzyltau sandstones. Thus, they are not described again here. A comparable approach to matrix correction was likewise implemented for the sandstones in this region. After matrix correction, the average framework components are $Q_{69.4}F_{3.3}L_{27.3}$ (assigned to metamorphic lithics) and $Q_{69.4}F_{9.6}L_{21.0}$ (assigned to feldspars), with the lithic composition comprising $Lv_{16.4}Lm_{61.8}Ls_{21.8}$ (assigned to metamorphic lithics; Fig. 4D).

Depositional Age

The presence of coal seams in the southwestern Tarim Basin is a possible proxy for the Jurassic system (Zhong et al., 2002). Although this proxy is limited by the lack of chronological data, it still retains indicative value. Approximately 30 km northeast of the Oytag section, Liu (2002) conducted a detailed pollen analysis of two samples derived from the J_2t strata (Table S5). The analysis indicated a prevalence of *Cyathidites minor*, *Classopollis annulatus*, *Pseudopicea variabiliformis*, and *Abietineaepollenites pectinellus*, which collectively suggest a stratigraphic age spanning from the Triassic to the Early Cretaceous.
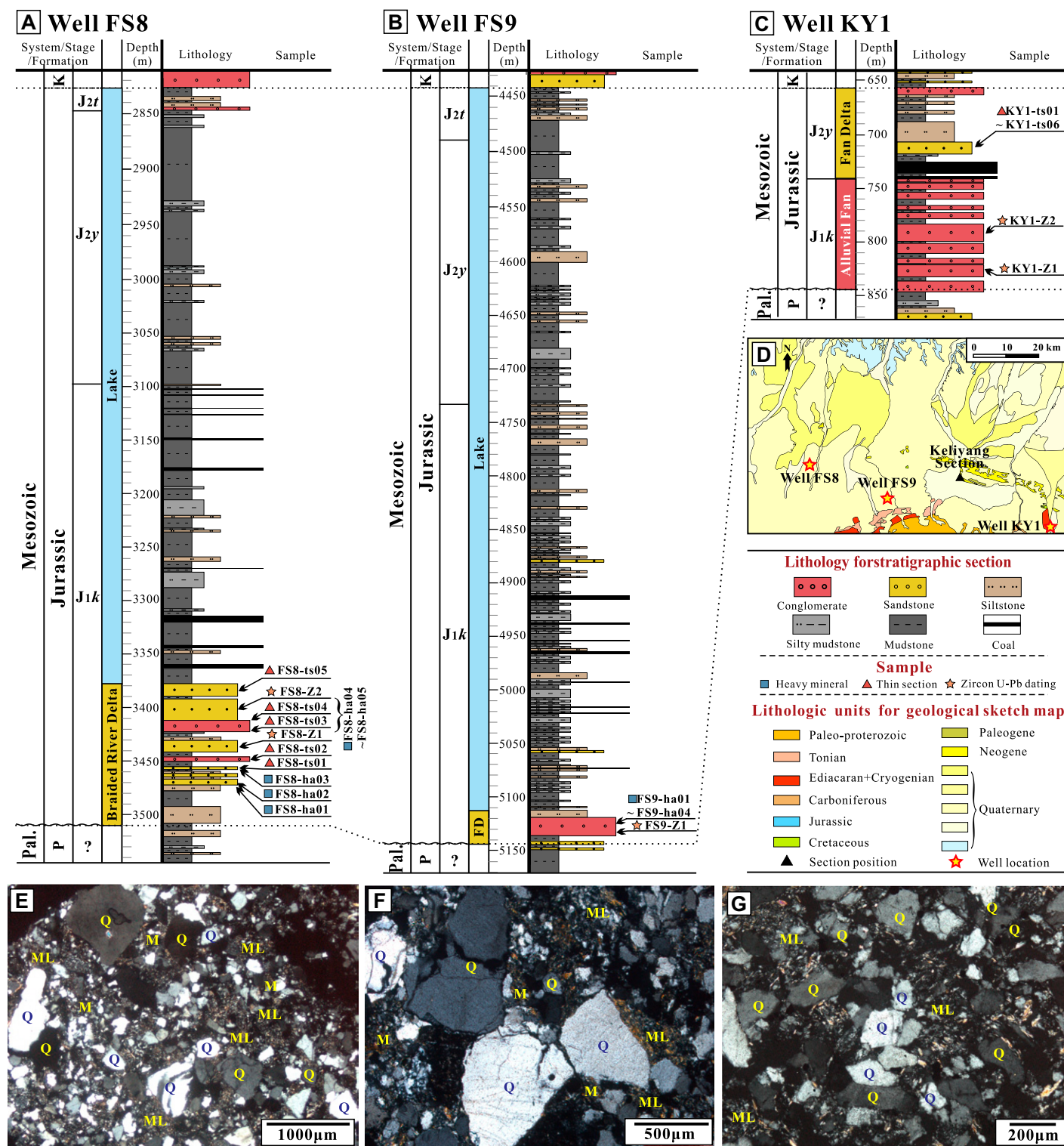
Figure 7. Composite stratigraphic section of the Jurassic strata from (A) Well FS8, (B) Well FS9, and (C) KY1 in the Fusha region. (D) Panel at right shows a detailed geological map around the Fusha region. See Figure 1B for the location of the Fusha region. (E) Quartz grains are composed of monocrystalline grains and polycrystalline grains (from sample KY1-ts03, 714.0 m, taken in cross-polarized light [XPL]). (F) Microscopic features of quartz, metamorphic lithics, and matrix (from sample FS8-ts05, 3378.5 m, XPL). (G) Microscopic features of quartz and metamorphic lithics (from sample KY1-ts05, 706.0 m, XPL). F—feldspar; FD—fan delta; M—matrix; ML—metamorphic lithics; Q—quartz; Pal.—Paleozoic; P—Permian; K—Cretaceous.

In the absence of a precise depositional age for the Jurassic strata of the southwestern Tarim Basin, the following evidence suggests a depositional period ranging from the Toarcian to the Bathonian: (1) Rb-Sr dating of red rhyolitic crystal tuffs located ~40 km southwest of the Oytag section yielded an age of 180 ± 10 Ma (Arnaud, 1992). The presence of similar volcanic detritus within the Jurassic basal conglomerates at the Oytag section suggests a maximum depositional age that is approximately contemporaneous with the Toarcian (Sobel, 1999). (2) Outcrops of sandstone-hosted copper deposits in J_3k sedimentary rocks are located ~50 km north of the Qimgan section, in the Sarekebayi subbasin. The chalcopyrite has been dated to 166.3 ± 2.8 Ma using the Re-Os geochronometric method (Fang et al., 2018), indicating a minimum depositional age that is approximately coeval with the Bathonian.

HEAVY MINERAL ASSEMBLAGES

The relative percentages of heavy minerals in the sandstone samples are plotted as a heatmap for optimal clarity (Fig. 8). Overall, the most prevalent heavy minerals are ilmenite, zircon, tourmaline, and garnet, present in 100%, 100%, 72.2%, and 61.1% of the samples analyzed, with median concentrations of 67.9%, 20.5%, 3.4%, and 2.5%, respectively. Other transparent heavy minerals include rutile, apatite, epidote, and titanite.

Based on an analysis of the heavy mineral assemblages using a heatmap, MDS plot, and tourmaline-garnet-epidote triangular diagram, two primary clusters were identified (A and B, Figs. 8A–8C). Cluster A comprises the Qimgan and Oytag sections (n = 6), while Cluster B includes the Toyunduk-Kyzyltau section and Fusha region (n = 12). These clusters exhibit pronounced differences in the proportions of ilmenite, tourmaline, garnet, and epidote. Samples in Cluster A display relatively low ilmenite content (6.3%–67.6%, with a median of 47.9%), with relatively higher concentrations of garnet (8.8%–34.4%, with a median of 16.6%), as well as a minor but notable presence of epidote. Samples in Cluster B exhibit a relatively high concentration of ilmenite, ranging from 64.2% to 91.2% with a median of 77.1% and contain varying proportions of tourmaline, from 2.1% to 15.2% with a median of 6.0%, while garnet is scarcely detectable. In terms of heavy mineral indices, samples in Cluster A contained GZI values ranging from 18.9 to 55.2 and ZTR values from 20.7 to 57.8, whereas samples in cluster B possessed GZI values from 0 to 24.0 and ZTR values from 8.8 to 31.7, both significantly lower than those of samples in Cluster A (Figs. 8D and 8E).

DETRITAL ZIRCON U-Pb GEOCHRONOLOGY

Zircon Morphologies and Th/U Ratios

A total of 2500 zircon grains were extracted from 10 sandstone samples for morphological characterization, and 1150 representative grains were selected for subsequent element analysis and U-Pb dating. The zircon grains exhibited a range of sizes, with cross-sectional diameters predominantly between ~60 μm and 300 μm. The smaller grains tended to be equant, whereas the larger grains were typically elongated, reaching maximum aspect ratios of 1:5. The majority of zircon grains displayed a stubby prism morphology with angular to subangular features. CL imaging revealed that most of the zircons exhibited oscillatory, sector, or irregular concentric internal zoning, which was occasionally truncated by a new or recrystallized growth zone (Fig. 9), indicative of an igneous origin (Corfu et al., 2003). Approximately 10% of the zircon fraction is lighter in color and exhibits either weak oscillatory zoning or metamorphic accretion textures, such as those observed in Figures 9C (#70) and 9E (#48), among others.

The Th/U ratios of the detrital zircons from the Jurassic strata spanned from 0.02 to 6.67, with a concentration of values between 0.2 and 1.3 (Fig. 10). A significant proportion of the grains, 82.1% (944 out of 1150), had Th/U ratios >0.4, suggesting that these zircons originated from igneous protoliths (e.g., Corfu et al., 2003; Linnemann et al., 2011). Only 10 zircons out of the 1150 grains that presented Th/U ratios of <0.1 are interpreted to be aqueous-fluid-precipitated overgrowths or metamorphic in origin (Liati et al., 2002; Grant et al., 2009). Certainly, Th/U ratios <0.1 do not entirely preclude the possibility of magmatic growth, especially where modest degrees of partial melting lead to relative enrichment of U over Th (Williams, 2001).

Detrital Zircon U-Pb Geochronology

The detrital zircon U-Pb age data from 27 modern river samples (Fig. 11) and 10 J_1s–J_2t sandstone samples (Fig. 12) are presented as percentage components in probability density plots (PDPs) and pie charts (Fig. 12). To evaluate the spatial variation in Jurassic provenance, this work also compiled detrital zircon U-Pb data from previous studies for four J_1s–J_2t samples: one from the Oytag section (Bershaw et al., 2012) and three from the Toyunduk-Kyzyltau and Kandilik sections (Fig. 12; Wu et al., 2025).

For sample QM-Z1, the majority of zircon grains cluster between ca. 250 Ma and 225 Ma,

with a prominent peak at 235 Ma. Additionally, minor age populations between 1000 Ma and 600 Ma are discernible. The detrital zircon U-Pb analyses of sample QM-Z2 revealed a range of ages from 2893 Ma to 227.1 Ma, with the dominant ages being Triassic (ca. 240–227 Ma, with a major peak at 233 Ma), and subordinate ages being Neoproterozoic (ca. 680–600 Ma and 1000–930 Ma). Sample QM-Z3 contains a prominent group of detrital zircons with ages of ca. 240–215 Ma, with a peak at 223 Ma, as well as two individual subpopulations ranging from ca. 450 Ma to 420 Ma and from 950 Ma to 800 Ma.

Two sandstone samples, OY-Z1 and QY-Z2, were collected from the Oytag section (Fig. 5A). They exhibit slightly distinct age distributions (Fig. 12). The predominant age populations of sample OY-Z1 are distributed between ca. 260 Ma and 200 Ma, with a notable peak at 226 Ma, and another significant grouping between ca. 450 Ma and 385 Ma, culminating at 399 Ma. Additional minor age clusters are observed at ca. 300 Ma and 331 Ma. Sample OY-Z2 predominantly displays Triassic and late Paleozoic age populations, featuring a pronounced peak at 251 Ma, and two subordinate peaks at 302 Ma and 351 Ma. Furthermore, sample PMR-25 from a previous study (n = 86; Bershaw et al., 2012) exhibits age patterns broadly congruent with those of sample OY-Z2.

This study presents only a concise review of the J_1s–J_2t strata in the Toyunduk-Kyzyltau and Kandilik sections because the datasets were provided by Wu et al. (2025). The age distributions of detrital zircons exhibit strikingly consistent population patterns, characterized by main peaks in the early Silurian (ca. 450 Ma) and Tonian (ca. 800 Ma). This similarity suggests that the sediments from the two outcrops originated from a common exhumed provenance (Wu et al., 2025).

Five sandstone samples, designated as FS8-Z1, FS8-Z2, FS9-Z1, KY1-Z1, and KY1-Z2, were extracted from three wells in the Fusha region (Figs. 7A–7C), exhibiting largely consistent age patterns (Fig. 12). The zircon age spectra of samples FS8-Z1 and FS8-Z2 reveal a straightforward pattern, with primary age peaks concentrated at ca. 480–420 Ma and 850–750 Ma. Moreover, both samples contain a minor, yet significant, proportion of Mesozoic, Mesoproterozoic, Paleoproterozoic, and Archean zircons. Sample FS9-Z1 is characterized by a high abundance of Paleozoic (ca. 460–410 Ma) and Neoproterozoic (ca. 850–730 Ma) zircons, with notable peaks at 430 Ma and 784 Ma. It also includes a minor, but noteworthy, component of Mesoproterozoic, Paleoproterozoic, and Archean zircons. Samples KY1-Z1 and KY1-Z2 exhibit a pronounced unimodal age peak at ca.
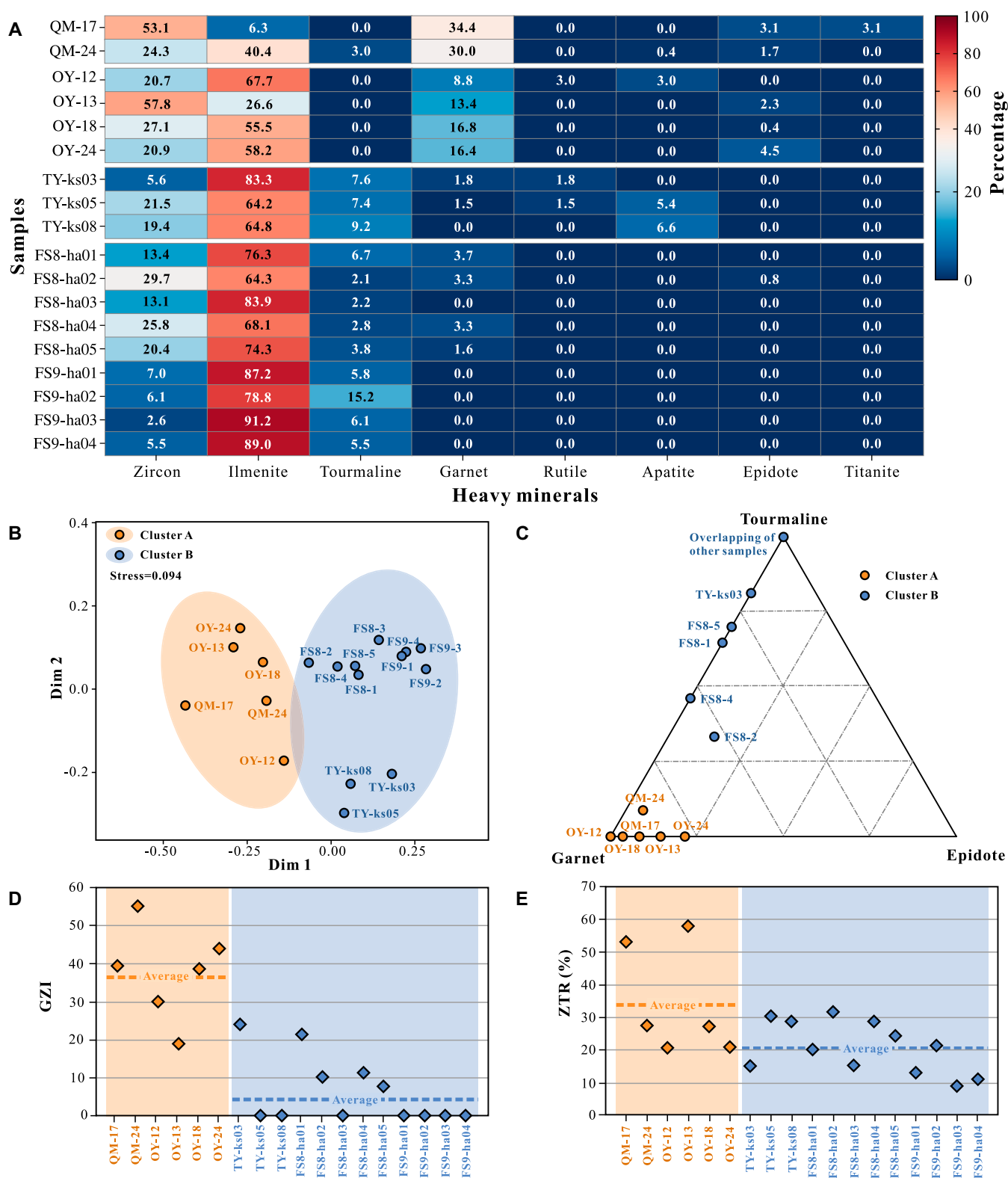
Figure 8. (A) Heatmap displaying the relative abundance of heavy minerals within the sandstone samples to facilitate optimal observation. Cluster analysis identified two primary clusters: Cluster A (Qimgan and Oytag sections, n = 6) and Cluster B (Toyunduk-Kyzyltau section and Fusha region, n = 12). See Figures 3–7 for the specific locations of the samples. (B) Multidimensional scaling plot of heavy minerals from the Jurassic sandstones. The stress value of 0.094 indicates a good fit. (C) Ternary plots for the tourmaline, garnet, and epidote. (D) Provenance-sensitive heavy mineral Garnet Zircon Index (GZI; Morton and Hallsworth, 1994) displayed on the scatter plot. (E) Ultrastable heavy mineral Zircon-Tourmaline-Rutile Maturity Index (ZTR; Hubert, 1962) displayed on the scatter plot.
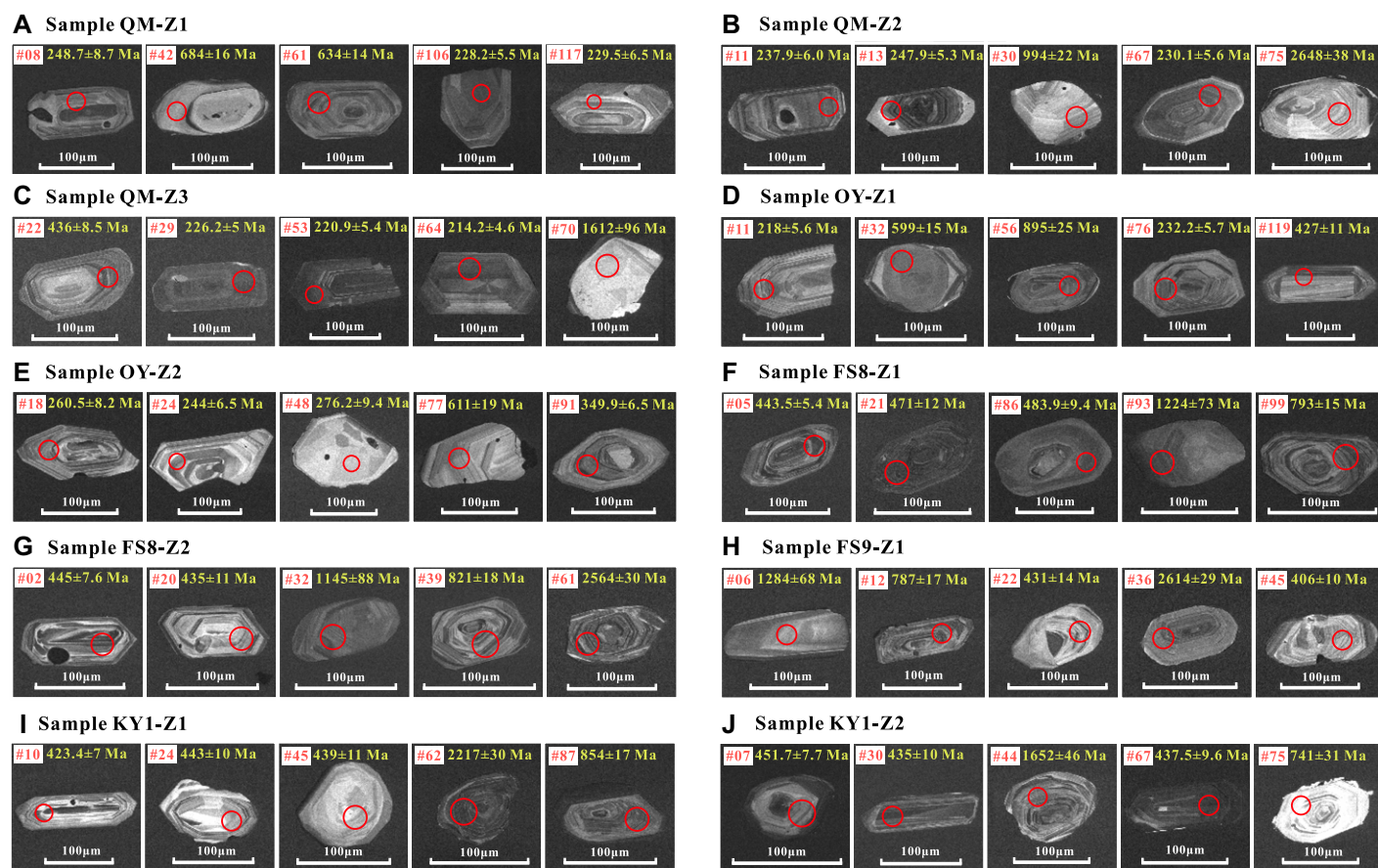
Figure 9. Cathodoluminescence (CL) images of representative zircon grains from the Jurassic sandstones. Red circles on the zircons indicate the analytical spots for U-Pb dating, and numbers represent the corresponding U-Pb ages.

450 Ma, accompanied by a distinct subpopulation that peaks at ca. 820 Ma (Fig. 12).

PROVENANCE INTERPRETATION

Thin-Section Observation

The mean framework components, lithic compositions, and optical characteristics of the sandstones within the Qimgan and Oytag sections exhibit a significant similarity (Fig. 4). Such intimate correspondence suggests a considerable degree of provenance similarity. The presence of well-preserved volcanic lithics suggests that diagenetic processes have exerted only a minor influence on the original composition of the rock (Panca et al., 2024). The irregularly shaped quartz crystals with sharp edges and corroded embayments suggest a volcanic origin, which is atypical of most fluvial or eolian terrigenous detritus (Figs. 3A and 5A; Bohor and Triplehorn, 1993). The latter typically exhibits significant sorting and rounding characteristics, along with a blurred surface texture. The oscillatory zoning and corroded embayments in plagioclase,

along with the widespread occurrence of volcanic lithics, are definitive hallmarks of a volcanic provenance (Figs. 3G, 3H, and 5F–5H; Pittman, 1970). However, it should be noted that plagioclase's oscillatory zoning can also originate from granitoid sources. Given the widespread occurrence of volcanic lithics and the relatively low abundance of granitoid lithics, the North Pamir

Triassic granitoids are unlikely to have been the dominant source, but may have provided a minor contribution to the sediment supply (Fig. 1B). Accordingly, the evidence presented leads us to favor the interpretation of the provenance as being primarily of volcanic origin.

For the Toyunduk-Kyzyltau section and Fusha regions, following matrix correction, all
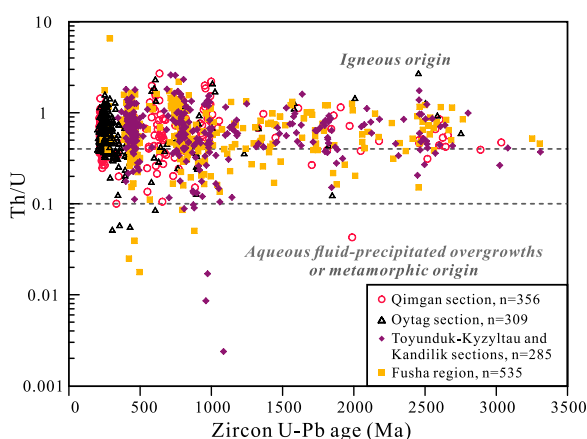

Figure 10. Th/U ratios of detrital zircon grains from age-dated Jurassic sandstone samples sourced from the southwestern Tarim Basin. Ratios >0.4 likely indicate an igneous origin (Corfu et al., 2003; Linnemann et al., 2011), and those <0.1 are most likely linked to aqueous fluid-precipitated or metamorphic origins (Liati et al., 2002; Grant et al., 2009). Samples in the Toyunduk-Kyzyltau and Kandilik sections are from Wu et al. (2025).
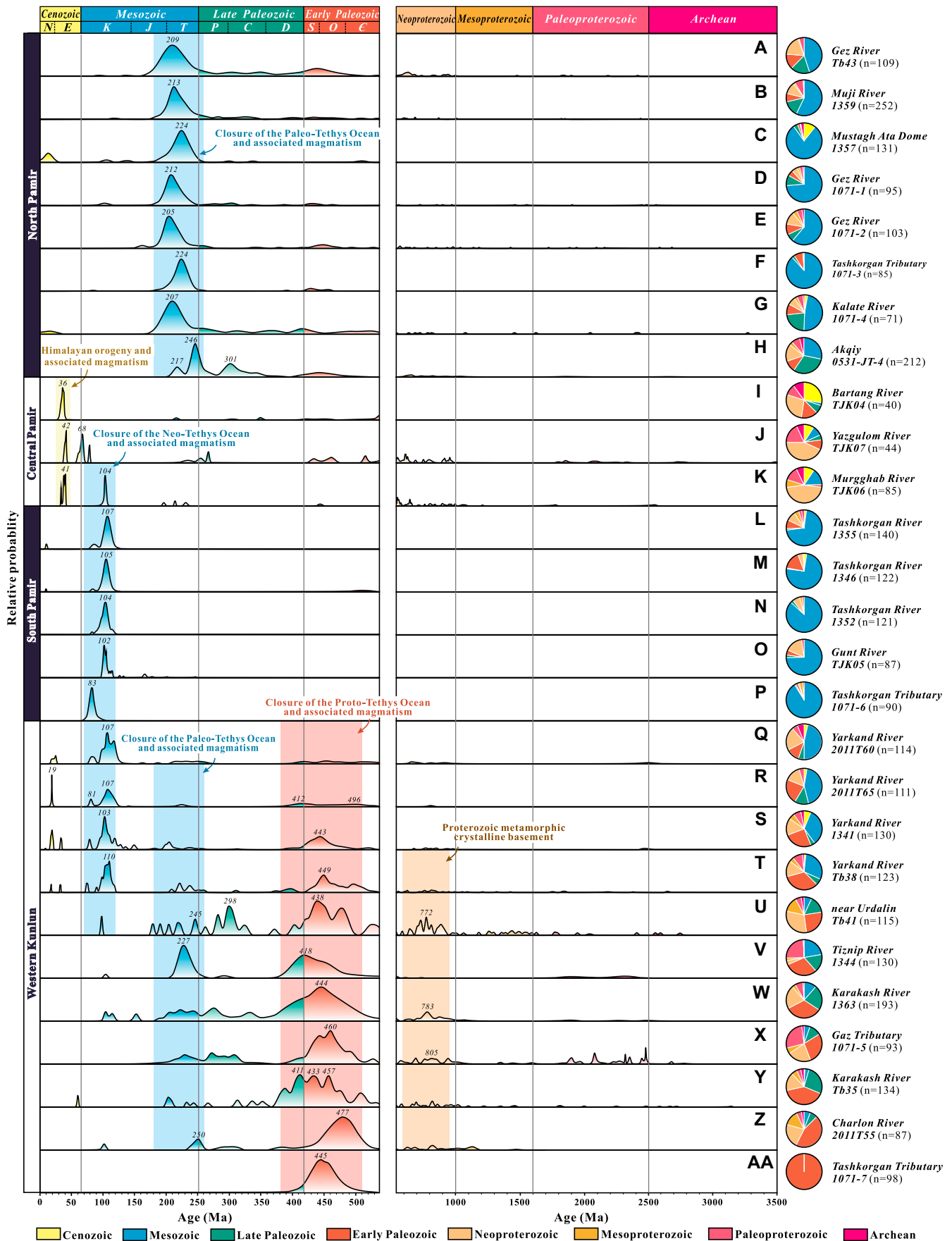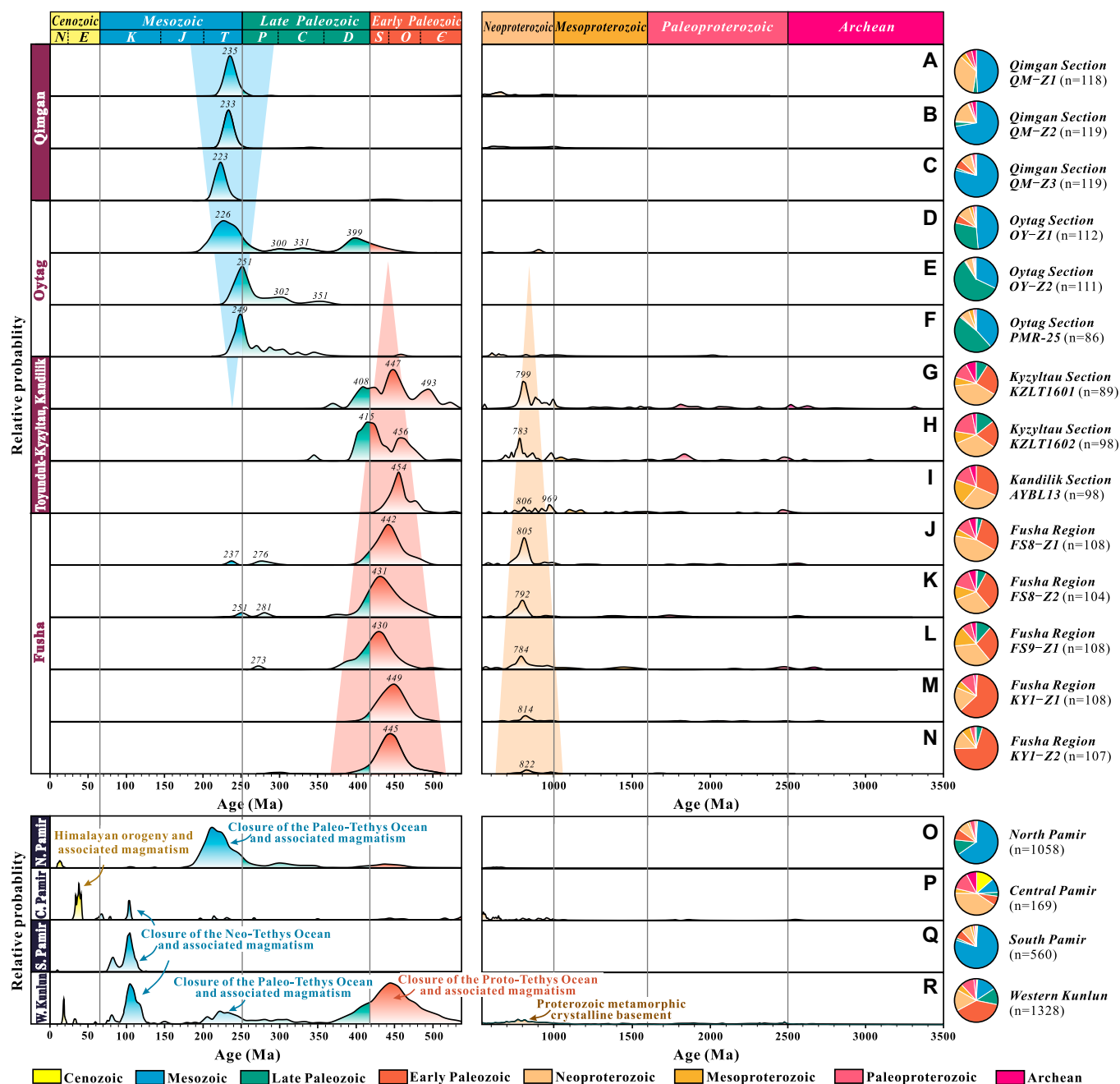
Figure 11. Normalized probability density plots for U-Pb detrital zircon data from modern rivers draining the Western Kunlun, South Pamir, Central Pamir, and North Pamir terranes. The shaded bars highlight the data for ca. 950–600 Ma (typical of Western Kunlun provenance of Proterozoic metamorphic crystalline basement), ca. 510–380 Ma (typical of Western Kunlun provenance triggered by the closure of Proto-Tethys Ocean), ca. 260–180 Ma (typical of Western Kunlun and North Pamir provenance triggered by the closure of the Paleo-Tethys Ocean), and ca. 120–70 Ma (typical of Pamir provenance triggered by the closure of the Neo-Tethys Ocean). The peaks serve merely as a reference for the age distribution range, with no quantitative significance. References: (A, T, U), Rittner et al. (2016); (B, C, L–N, S, V, W), Blayney et al. (2016); (D–G, P, X, AA), Carrapa et al. (2014); (H, Q, R, Z), Liu et al. (2017); (I–K, O), Lukens et al. (2012). N—Neogene; E—Paleogene; K—Cretaceous; J—Jurassic; T—Triassic; P—Permian; C—Carboniferous; D—Devonian; S—Silurian; O—Ordovician; Є—Cambrian.

Figure 12. Normalized probability density plots for U-Pb detrital zircon data from the Jurassic sandstones in the southwestern Tarim Basin are compared to the age probability curves from modern rivers draining the Western Kunlun, South Pamir, Central Pamir, and North Pamir terranes. Data are from this study except where noted. Data sources: Sample PMR-25 is from Bershaw et al. (2012), and samples KZLT1601, KZLT1602, and ABYL13 are from Wu et al. (2025). N—Neogene; E—Paleogene; K—Cretaceous; J—Jurassic; T—Triassic; P—Permian; C—Carboniferous; D—Devonian; S—Silurian; O—Ordovician; Є—Cambrian.

Geological Society of America Bulletin

data points predominantly plot within the fLQ, LQ, and Qu fields, likely reflecting the source characteristics of schists and paragneisses (Garzanti et al., 2010). The substantial number of quartz grains and the prevalence of metamorphic lithics (phyllite, schist, and gneiss) imply that the provenance is largely attributable to a metamorphic or granitoid source (Figs. 4C, 4D, 6, and 7), markedly divergent from the characteristics exhibited by the parent volcanic rocks of the Qimgan and Oytag sections. This suggests that the sandstones in the region may be linked to the provenance supply from metamorphic complexes and granitoids of the Western Kunlun Shan region (Fig. 1B). The enhanced diagenetic alteration is considered a plausible explanation for the diminished feldspar content observed within the rocks. Following this alteration, the feldspar grains experienced a marked reduction in compaction resistance, which ultimately resulted in their transformation into pseudomatrix.

Although grain-size variations are observed among the sandstones, the framework component and lithic composition remain broadly consistent when compared within each individual region (Fig. 4). The compositional similarity across grain-size fractions is likely a result of the proximal, high-energy depositional settings—alluvial fans and braided river deltas (Table S4). In these environments, two factors contributed to the similarity: (1) a compositionally uniform and stable source area that strongly controlled the sediment supply and (2) relatively rapid sedimentation rates (Wu et al., 2021). Such sediments are typically eroded, transported, and deposited over short distances, resulting in frequently fluctuating hydrodynamic conditions but insufficient time and spatial extent for effective mineralogical sorting. These two factors may collectively explain the limited compositional variation observed among sandstones with different sizes.

Heavy Mineral Assemblage Aspect

The analysis revealed fluctuations in tourmaline abundance and GZI values (garnet abundance) between Clusters A and B, indicative of a different sedimentary provenance. Tourmaline, a weathering-resistant heavy mineral, is predominantly found in aluminum-enriched granites and their associated pegmatites, as well as in high-grade metamorphic rocks, such as gneiss, amphibolite, and mica schist (Henry and Dutrow, 1996). This implies that the source rocks of samples in Cluster B were likely derived from Precambrian metamorphic complexes and Paleozoic and Triassic granitoids situated within the North Kunlun and South Kunlun regions

(Fig. 1B), which is consistent with the results obtained from the observation of lithics (Figs. 4, 6, and 7). From a petrological perspective, we infer that the provenance of Cluster A samples is predominantly linked to mafic volcanic eruptions. Nevertheless, garnet is generally absent in basaltic magmas, given its instability under the low-pressure crystallization conditions. Therefore, we advance the hypothesis that although the principal source is probably associated with mafic volcanic activity, there may also be small contributions from other source regions. The Muji–Bulunkou area, located southwest of the Qimgan and Oytag sections, contains widespread exposures of Triassic garnet-bearing Li-Be pegmatites and strongly peraluminous granites (Fig. 1A). These rocks, along with their garnet-rich wall rocks (schists of the Bulunkuole Group), may have served as a potential source of detrital garnet (Yan et al., 2022). The concurrent occurrence of minor epidote with the ZTR fraction also implies that there may be additional contributions from other source regions (Glazer et al., 2023).

Detrital Zircon U-Pb Dating

How Faithfully Does the Modern River Signal Reflect the Jurassic Source Terranes?

As reported in previous publications, detrital zircon U-Pb age data were acquired from 11 modern river sand samples derived from the Western Kunlun Shan region and 16 samples sourced from the Pamir region to delineate the geochronological signature of potential sediment provenances (Fig. 11; Lukens et al., 2012; Carrapa et al., 2014; Blayney et al., 2016; Liu et al., 2017). Throughout the Triassic–Jurassic, the Central Pamir and South Pamir terranes experienced extensive continental–marine transitional sedimentation (Fig. 1B; Rutte et al., 2017; Villarreal et al., 2020), and a Triassic–Jurassic basin is believed to have been situated between the North Pamir and Central Pamir terranes (Rembe et al., 2022), which was a consequence of the closure of the Paleo-Tethys Ocean (Schwab et al., 2004; Imrecke et al., 2019). This basin is likely analogous to the trough that accommodated a shallow sea, which spanned from the Band-e Bayan Block in Afghanistan to the west (Girardeau et al., 1989) and Central Pamir to the eastern Tianshuihai Terrane along the southern flanks of the Western Kunlun Shan region (Zhang et al., 2019b). This geological setup may have acted as a barrier to northward sediment transport from the Central and South Pamir terranes during the Jurassic. Furthermore, the detrital zircons from Central Pamir and South Pamir terranes are distinguished by age peaks corresponding to the Cretaceous–Paleogene (Fig. 11; Lukens et al.,

2012; Carrapa et al., 2014). Consequently, the results here align with the view of Zhang et al. (2019b), who proposed that the Western Kunlun Shan region and North Pamir Terrane constituted the principal source areas for the Jurassic sediments in the southwestern Tarim Basin, with minimal contributions from the Central Pamir and South Pamir terranes.

In summary, the detrital zircon population from the Western Kunlun Shan region (n = 1328) exhibits age groups ranging from ca. 950 Ma to 600 Ma, from 510 Ma to 380 Ma, from 260 Ma to 180 Ma, and from 120 Ma to 70 Ma (Fig. 11). Conversely, the North Pamir Terrane displays a tightly clustered age distribution of detrital zircons (n = 1058), predominantly between ca. 230 Ma and 190 Ma.

Several lines of evidence were presented to support the fidelity of the modern river signal as a proxy for the Jurassic source terranes: (1) The magmatism within the Western Kunlun Shan region and North Pamir Terrane may have been either entirely absent or significantly subdued following the Jurassic, suggesting minimal Cretaceous and Cenozoic impact on the Jurassic source signal. (2) The Western Kunlun Shan–Pamir Paleo-Tethys Realm, particularly the North Kunlun–South Kunlun and North Pamir terranes, underwent significant thickening and uplift prior to the Jurassic due to the closure of the Paleo-Tethys Ocean (e.g., Bershaw et al., 2012; Villarreal et al., 2020), with postcollisional orogeny maintaining minimal source terrane changes. (3) Sobel (1999) posited that the Jurassic deposits in the southwestern Tarim Basin originated mainly from the Pamir region's eastern margin and the westernmost Kunlun region, resembling modern intermontane river systems in the southwestern Tarim Basin. However, we acknowledge that the signal from modern river sands should be interpreted with care and may necessitate revision as additional data are acquired.

Spatial Differentiation of Detrital Zircon U-Pb Signals

The 3-D MDS clustering (Fig. 13) correlates strongly with the heavy mineral analysis (Fig. 8). The samples from the Qimgan and Oytag sections and North Pamir provenance form a relatively compact cluster (Group A). In contrast, a separate cluster is formed by the samples from the Toyunduk-Kyzyltau section, the Fusha region, and Western Kunlun Shan provenance (Group B).

A visual analysis of PDPs suggests that Group A is very similar to modern river sands derived from the North Pamir Terrane (Fig. 12). The samples from both the Qimgan and Oytag sections are predominantly characterized by Tri-
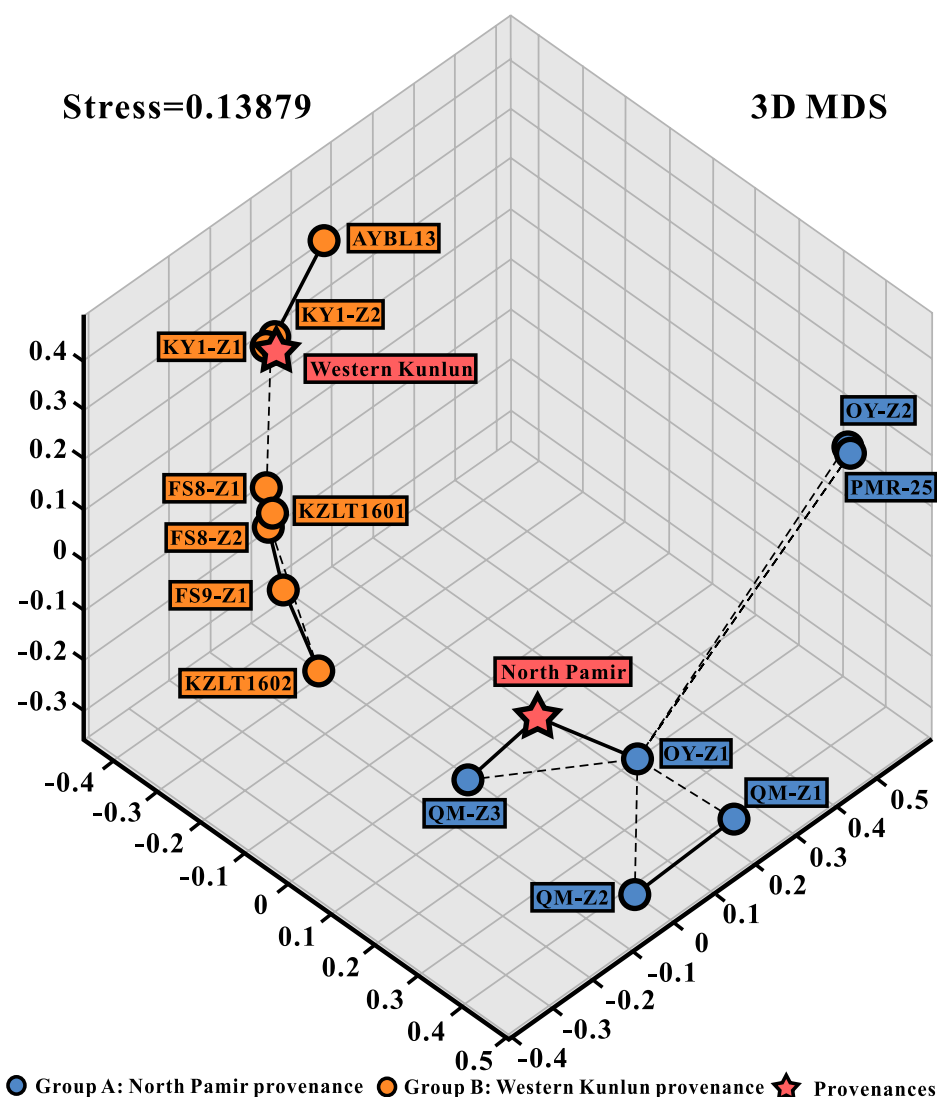
Figure 13. Three-dimensional multidimensional scaling (3-D MDS) plots depicting the detrital zircon age data from both Jurassic sandstones and modern river sands that drain the Western Kunlun and North Pamir terranes.

a more important and previously underappreciated source within the North Pamir Terrane.

Unsurprisingly, the provenance of Group B is inextricably linked to the rock units of the Western Kunlun Shan region. Considering the geological map and prior research, the likely sediment sources for Group B include the North Kunlun, South Kunlun, Tianshuihai, and Songpan-Ganzi terranes (Fig. 1B). The PDPs of all samples within Group B exhibit identical dominant age modes, ranging from 850 Ma to 750 Ma and from 450 Ma to 400 Ma. These ages correspond to the Precambrian metamorphic complex and the extensive Ordovician–Devonian granitoids exposed in the current North Kunlun and South Kunlun terranes (e.g., Zhang et al., 2018; Yin et al., 2020). The absence of Triassic–Jurassic detrital zircons in the Fusha region suggests that no fluvial system existed during the Jurassic that could have transported sediments across the intervening Western Kunlun Shan region—a prominent mountain range—linking the Tianshuihai and Songpan-Ganzi terranes to the Fusha region. Samples KZLT1601 and KZLT1602, however, present a relatively complex age spectrum, including minor late Paleozoic age populations (Figs. 12G and 12H), indicating that there may have been additional provenance inputs alongside the primary North Kunlun–South Kunlun source. The mixed provenance of these two samples likely included contributions from the proximal bimodal volcanism along the northeastern margin of the North Pamir Terrane. Consequently, the proximal sources of the North Kunlun–South Kunlun terranes were the principal contributors to the Jurassic sediments in Group B, with minor contributions from late Paleozoic bimodal volcanic sources in the Toyunduk-Kyzyltau section.

Overall Provenance

Taken together, the Jurassic sediments exhibit clear characteristics of sedimentation from proximal sources. The sediments in Qimgan and Oytag are predominantly sourced from nearby Triassic volcanic rocks, which may have been extensively eroded and are observed only in a few outcrops (Rembe et al., 2022). Although there is a potential contribution from the Triassic granitoid batholiths in the North Pamir Terrane, they do not appear to represent the main source. The subpopulations of late Paleozoic detrital zircons in the Oytag and Toyunduk-Kyzyltau regions suggest sediment input from the bimodal volcanic sequence exposed along the northeastern margin of the North Pamir Terrane. The proximal sources of the North Kunlun–South Kunlun terranes (Precambrian metamorphic complexes and Paleozoic granitoids) were the principal contribu-

assic age populations, with those in the Oytag section also exhibiting late Paleozoic age populations (Fig. 12). Based on the current geological map and previous studies, three potential provenance domains in the North Pamir Terrane are considered for the Jurassic sands: late Paleozoic volcanic rocks, Triassic granitoid batholiths, and limited Triassic volcanic rocks. The source of the late Paleozoic detrital zircons is not in question and is generally attributed to bimodal volcanism induced by the northward subduction of the Paleo-Tethys Ocean along the northeastern margin of the North Pamir Terrane (e.g., Ji et al., 2017; Rembe et al., 2021; Song et al., 2024). These signatures are consistent with the igneous zircon ages (354–264 Ma) observed in the widely distributed volcanic rocks along the

northeastern margin of the Pamir Plateau (e.g., Zhang et al., 2006; Jiang et al., 2008; Rembe et al., 2021; Mu, 2016; Huangfu, 2018). As for the Triassic detrital zircons, existing hypotheses predominantly support a provenance from the granitoid batholiths that formed in response to the closure of the Paleo-Tethys Ocean and the subsequent continent–continent collision (Schwab et al., 2004; Imrecke et al., 2019; Zhang et al., 2019b). However, this interpretation is not fully consistent with the robust petrological evidence (the dominance of volcanogenic minerals, such as high-temperature quartz and basaltic lithics; Fig. 3) within the Qimgan-Oytag sandstones, which strongly suggests a volcanic provenance. The aforementioned evidence suggests that the localized Triassic volcanic rocks may be

tors to the early Paleozoic and Neoproterozoic sediments in Toyunduk-Kyzyltau and Fusha.

TECTONIC IMPLICATIONS

The Significance of Triassic Volcanic Eruptions

The Triassic volcanic activity in the northeastern Chinese Pamir region has been the subject of only limited prior attention, in contrast to the more thoroughly documented Triassic volcano-sedimentary sequences of the Afghanistan-Kyrgyzstan Pamir region. Rembe et al. (2022) provided a detailed delineation of the Triassic volcanic activity within the Hindukush Mountains in Afghanistan and the northwestern Pamir region in Tajikistan and Kyrgyzstan. Here, the key contents of their synthesis are summarized succinctly: (1) Felsic volcanic rocks ranging from Anisian to Ladinian in age are present along the northwestern flank of the Hindukush Mountains in northern Afghanistan (Wolfart and Wittekindt, 1980). Furthermore, the intercalation of lava flows (dated to the Norian age using K-Ar radiometric dating) with terrigenous sandstones in the region, particularly in the Doab area of northern Afghanistan (Fig. 2A), attests to the extensive Triassic synsedimentary volcanism (Blaise et al., 1970). This setting is commonly interpreted as a backarc basin, linked to the Paleo-Tethys oceanic subduction and volcanic arc activity (Siehl, 2017). (2) In the Altyn Darya Valley of the Kyrgyzstan North Pamir Terrane (Fig. 2A), the prevalence of Rhaetian-aged chemically immature volcanic clasts within a thick sequence of continental clastic deposits (~2500 m) also signals a period of intense Triassic synsedimentary volcanism (Budanov, 1993). This volcano-sedimentary succession is understood to be the product of a short-lived backarc extensional basin (Salikhov and Sakiev, 2014).

Of greater significance, Rembe et al. (2022) reported outcrops of Triassic pyroclastic rocks ~5 km northwest of the Qimgan section, dated to 244.1 ± 1.1 Ma, and a similar unit in the Gez Valley (near the Oytag section) dated to 233.4 ± 1.1 Ma. Bulk-rock geochemical analyses of these sequences suggest a volcanic backarc origin. Therefore, in light of the aforementioned results, Rembe et al. (2022) posits that there may have been a >1000-km-long realm of Triassic backarc extension to the north of the Paleo-Tethys subduction zone, extending across the northeastern Chinese Pamir region, the northwestern flank of the Hindukush Mountains, the Doab area in northern Afghanistan, and the Altyn Darya Valley of the Kyrgyzstan North Pamir Terrane.

In this study, the well-preserved Triassic volcanic lithics within the Jurassic deposits of the Qimgan-Oytag sections provide critical insights into the geodynamic crustal evolution of the North Pamir Terrane (Figs. 3–5). The detrital zircons dated from the Qimgan-Oytag sections constrain the age of the volcanic lithics to between ca. 250 Ma and 210 Ma (Figs. 12A–12F), aligning chronologically with the Triassic backarc magmatism in the Altyn Darya Valley of the Kyrgyzstan North Pamir Terrane and northern Afghanistan. This temporal correlation also coincides with the Karakul-Mazar granitoid batholiths of the North Pamir Terrane, within the context of the Paleo-Tethys oceanic subduction (Schwab et al., 2004; Robinson, 2015). Therefore, considering the temporal and tectonic relationships, the Triassic volcanic activity near the Qimgan-Oytag sections may also be attributed to backarc magmatism initiated by the closure of the Paleo-Tethys Ocean.

Based on the detrital zircon and petrological evidence presented in this study, we endorse the hypothesis posited by Rembe et al. (2022), suggesting that a northwest–southeast-trending Triassic backarc volcanic system was located in the northeastern Chinese Pamir region. This backarc volcanic system likely extended southward from Oytag, ultimately ceasing its development at an unspecified location between Oytag and Toyunduk-Kyzyltau. Furthermore, these volcanic rocks served as the parent rocks, providing detrital materials for the subsequent Jurassic deposits in the Qimgan and Oytag sections. This eruption event was kinematically linked to the backarc formation associated with the Paleo-Tethys oceanic subduction along the southern Asian continental margin. Owing to the significantly more labile nature of mafic volcanic rocks compared to granitoids, these rocks are likely to have undergone more intense and rapid erosion. Thus, the lack of volcanic rock outcrops from the current North Pamir Terrane may be attributed to the intense and thorough denudation that occurred as a result of the India-Asia collision and the substantial uplift of the Pamir-Tibet Plateau during the Cenozoic (Hacker et al., 2017). However, it must be emphasized that further studies on tectonics and igneous processes are necessary to fully elucidate the geodynamic history of this Triassic volcanic eruption.

Jurassic Tectonosedimentary Patterns

Scholars have debated the precise timing of the Western Kunlun Shan–Pamir Paleo-Tethyan collisional orogeny, with proposals ranging from the late Permian–Middle Triassic (e.g., Jiang et al., 2013; Liu et al., 2015) to the Late Triassic–Early Jurassic (e.g., Matte et al., 1996; Mattern and Schneider, 2000; Xiao et al., 2002; Wu et al., 2021). However, we align with the consensus that the orogeny, including the crustal thickening and uplift, had concluded prior to the Jurassic.

Figure 14 presents an idealized Jurassic depositional model for the southwestern Tarim Basin. Published isopach patterns indicate a Jurassic margin bounded by normal faults, parallel to the Western Kunlun Shan–Pamir Realm, which governed the sedimentation patterns and the variability in stratal thickness (e.g., Sobel, 1999; Wu, 2017). The initial stage, approximately corresponding to the J_1s and J_1k strata (Fig. 14A), is characterized by high-sediment-concentration floods that deposited proximal, coarse-grained alluvial fan–fan delta deposits (Figs. 3B, 3C, 5B, 6B, and 6C). The sediment transport pathways were dominated by hillslope mass wasting from the Western Kunlun Shan region (e.g., Toyunduk-Kyzyltau) and North Pamir Terrane (e.g., Qimgan-Oytag), conveyed through alluvial fan and intermontane river systems. Variations in potential provenance domains, preexisting topography, and the extent of surface deformation influenced by normal faults resulted in significant petrological variability and the spatial differentiation of detrital zircon U-Pb age distributions among individual outcrops and/or wells (Figs. 4 and 12).

Subsequent lateral propagation between fault segments may have led to the expansion and coalescence of early fault depocenters (Gawthorpe and Leeder, 2000; Fig. 14B). Isolated lakes may have become largely interconnected at this stage. Extensive lake and swamp sedimentation was the dominant feature during this stage (Figs. 6D, 6E, and 6J).

During the final stage, some areas show a parallel unconformable contact between the J_1s–J_2t and J_3k strata. According to Wu et al. (2021, 2025), this was likely induced by the northward subduction of the Neo-Tethys Ocean. The contractional event, governed by modifications in the subduction behavior of the Neo-Tethyan oceanic crust from southward retreat to northward flat-slab advance, led to the uplift of the Western Kunlun Shan–Pamir Realm, which profoundly influenced the tectonostratigraphic framework of the basin and altered the dynamics of its source-to-sink system. The inactivation of the main border fault and ongoing sediment supply may have led to the complete filling of the lacustrine basin (approximately corresponding to the J_3k strata, Fig. 14C). The sedimentary signatures record the reestablishment of alluvial fan and fan-delta deposition sourced from the Western Kunlun Shan region and North Pamir Terrane.

Possible Mechanisms of Jurassic Extension

The sedimentary facies in the study area exhibit a stratigraphic sequence from proximal
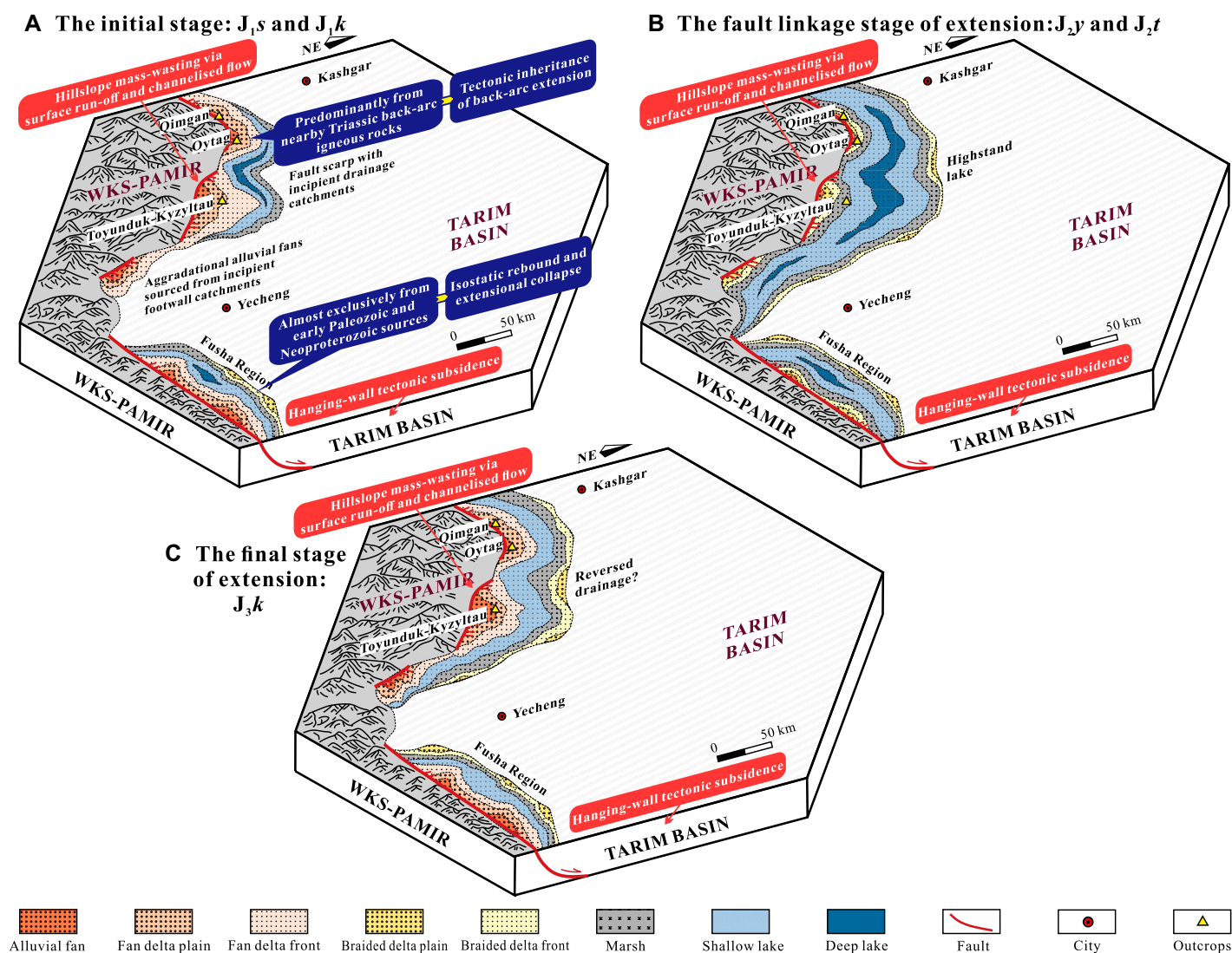
Figure 14. Schematic diagrams delineating the synthesized depositional model of the Jurassic in the southwestern Tarim Basin. The depocenters of the Jurassic basins generally trend north–northwest, aligning subparallel to the axis of the Western Kunlun Shan–Pamir Realm. The westward drainage patterns, formed through headward erosion, evolved across the Western Kunlun Shan (WKS)–Pamir Realm. This figure is adapted from Wu (2017). It illustrates three stages of extension: (A) the initial stage, approximately corresponding to the J_1s and J_1k strata; (B) the fault linkage stage of extension, approximately corresponding to the J_2y and J_2t strata; and (C) the final stage of extension, approximately corresponding to the J_3k strata.

alluvial fan to lacustrine deposits, terminating in coarse-grained alluvial fan deposits (Fig. 14). The observed facies pattern conforms to that proposed for extensional basin models (Gawthorpe and Leeder, 2000) and aligns with Sobel's (1999) proposition of several narrow, deep, and separated extensional grabens developing along the Western Kunlun Shan region and North Pamir Terrane during the Jurassic. Nevertheless, the diversity in detrital framework composition (Fig. 4), the distinct detrital zircon U-Pb age distributions (Fig. 12), and the basin scale suggest that the mechanisms governing extensional processes may exhibit variations.

The regional extension is primarily driven by backarc extension, continental rifting linked to mantle plumes, and postcollisional extension from lithospheric thinning (Zheng and Dai, 2018). There is no evidence of the Mesozoic mantle plumes recorded in or around the Tarim Basin. The Jurassic setting of the Qimgan and Oytag sections likely inherited the Triassic backarc extension, with the basin orientation adopting a northwest–southeast trend, aligned parallel to the Western Kunlun Shan–Pamir Realm axis. Evidence for this includes the following: (1) The zircon age populations exhibit a restricted distribution, with major peak ages

closely approximating the timing of sediment accumulation (Fig. 12). These spatial and temporal variations in sediment provenance are most plausibly attributed to basins located along plate margins with synsedimentary magmatic activity (Cawood et al., 2012), which aligns with the tectonic interpretations of the Triassic. (2) The sandstones are predominantly composed of mafic volcanic lithics and high-temperature quartz (Figs. 3–5), indicating a significant contribution of Triassic backarc eruption to the supply of Jurassic sediments.

In contrast, the Jurassic Toyunduk-Kyzyltau and Fusha regions are more likely to be inter-

preted as a rift basin that formed as a result of postcollisional extension, which was triggered by isostatic rebound. Evidence for this includes the following: (1) the Toyunduk-Kyzyltau and Fusha regions are distinguished by detrital zircon ages that significantly predate the depositional age (Fig. 12), indicating that the sediment supply was largely influenced by the stable presence of the provenance area, rather than by synsedimentary volcanic activity; (2) the sandstones, primarily composed of quartz with rough grain surfaces and high-grade metamorphic lithics (Figs. 4, 6,

and 7), similarly suggest a provenance that may have been relatively stable at a tectonic scale; and (3) a growing body of evidence suggests that a cooling event, significant crustal thickening, and the associated extensive surface uplift occurred across the Western Kunlun Shan region during the late Permian–Triassic (e.g., Matte et al., 1996; Kapp et al., 2007; Cao et al., 2015; Li et al., 2019a). This event may mark a stage in the region's tectonic evolution, in which the typical sequence of orogenic belt development in collisional settings was initiated—characterized

by crustal thickening, surface uplift, a period of tectonic quiescence, isostatic rebound, and finally extensional collapse (Wolf et al., 2022).

Moreover, previous studies of extensional basins in the southwestern Tarim Basin have revealed a structural configuration that aligns with the geometric and kinematic characteristics in Central Asia during the Mesozoic (Sobel, 1999). The northwest–southeast orientation—extending from Qimgan to Toyunduk-Kyzyltau—was broadly consistent with the regional stress field associated with the Talas-Ferghana
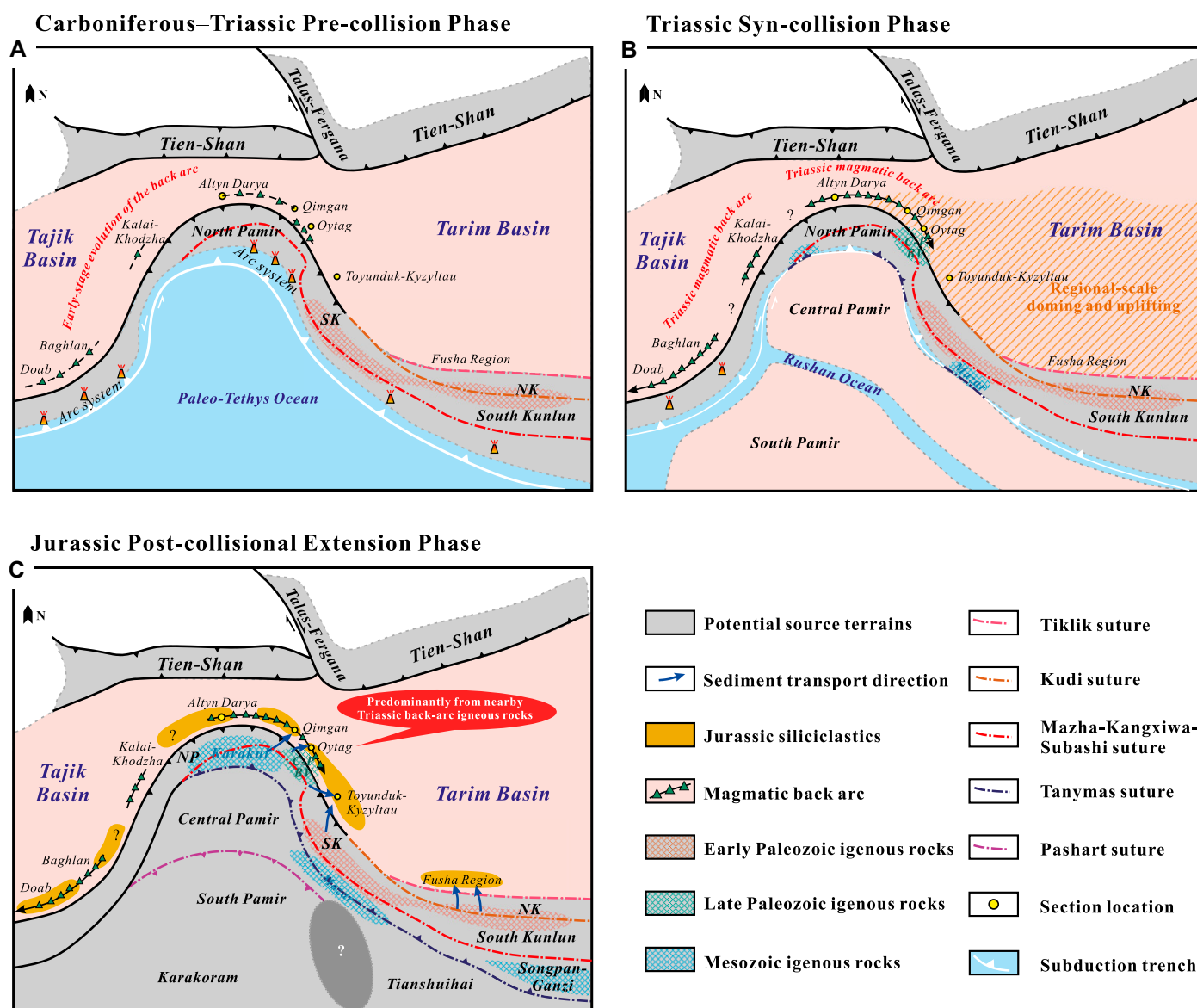

Figure 15. Schematic tectonic reconstructions illustrating the closure of the Western Kunlun–Pamir Paleo-Tethys Realm at key geological intervals, drawing inspiration from the works of Blayney et al. (2016), Yang et al. (2018), Li et al. (2020), and Aminov et al. (2023). The tectonic evolution encompassing the closure of the Western Kunlun–Pamir Paleo-Tethys Realm is conceptualized in three distinct phases: (A) the Carboniferous–Triassic precollisional phase, (B) the Triassic syncollisional phase, and (C) the Jurassic postcollisional phase. A comprehensive discussion of these phases is provided in the main text. C-PBV—Carboniferous–Permian bimodal volcanic sequence exposed along the northeastern North Pamir; NK—North Kunlun Terrane; NP—North Pamir Terrane; SK—South Kunlun Terrane.

fault, a major north-northwest–striking dextral strike-slip fault system active since the Mesozoic (Fig. 2A). Although the Talas-Ferghana fault is not the primary focus of this study, its role in shaping the regional stress regime during the Jurassic cannot be overlooked. These trends reflect structural weaknesses that localized deformation and guided the development of the basin. Therefore, the Qimgan-Toyunduk Jurassic Basin developed within an extensional regime that was closely related to the regional stress field governing the Talas-Ferghana fault. This result highlights the interplay between local fault development and tectonic processes.

Geodynamic Model

Carboniferous–Triassic Precollisional Phase

Since the Carboniferous, the northward subduction of the Paleo-Tethys Ocean initiated the development of an arc system and facilitated the early evolution of a backarc basin (Fig. 15A). Notably, in the southwestern Oytag section, this tectonic regime promoted the formation of a Carboniferous–Permian backarc basin, accompanied by the emplacement of bimodal volcanic rocks (Song et al., 2024). These volcanic sequences played a crucial role in supplying detrital material to the overlying Jurassic sedimentary succession of the Oytag section.

Triassic Syncollisional Phase

From a provenance perspective, the southwestern Tarim Basin can be divided into two tectonic domains: (1) the Paleo-Tethys–North Pamir, influencing the Qimgan to Oytag sections and (2) the Paleo-Tethys–Western Kunlun Shan, governing the Toyunduk-Kyzyltau section to Fusha region (Fig. 15B). For the Paleo-Tethys–North Pamir, the closure of the Paleo-Tethys Ocean led to the collision between the Qiangtang Terrane and the South Kunlun Terrane, causing intense uplifting and denudation of the southwestern Tarim Basin (Zheng et al., 2015; Xu et al., 2020). The scarcity of Triassic sediments is attributed to the northward tilting and regional uplift (e.g., McFadden et al., 1988; Zhu et al., 2013). In contrast, the Paleo-Tethys–North Pamir domain was characterized by an extensional backarc zone and calc-alkaline magmatic activity, initiated by the northward subduction of the Paleo-Tethys Ocean. This activity extended ~1000 km along the northern margin of the North Pamir Terrane (Blaise et al., 1970; Siehl, 2017; Rembe et al., 2022; Li et al., 2022), bridging the Doab area to the west and the Qimgan-Oytag area to the east. Shortly thereafter, an ~100-km-wide, collision-related granitoid belt, ranging from 243 Ma to 210 Ma in age (Wei et al., 2023), formed in the Karakul–

Mazar–Songpan-Ganzi region (Schwab et al., 2004; Robinson, 2015), indicating the final closure of the Paleo-Tethys Ocean.

Jurassic Postcollisional Extensional Phase

The basal Jurassic proximal alluvial fan deposits serve as a geological record of the waning stages of collisional orogeny, indicating that the closure of the Paleo-Tethys Ocean and the resultant primary collisional event had largely concluded prior to the Jurassic (e.g., Imrecke et al., 2019; Villarreal et al., 2020). Concurrently, the North Pamir and North Kunlun–South Kunlun terranes experienced pronounced uplift as a consequence of the collisional orogeny, effectively separating the distant sediment provenance of the Tianshuihai and/or Songpan-Ganzi and/or Central Pamir–South Pamir terranes either progressively or entirely. During this time, several narrow, deep, and separated postcollisional extensional grabens developed parallel to the southwestern margin of the Western Kunlun Shan and North Pamir Terrane. The structural configuration and northwest–southeast orientation of Jurassic extensional basins from Qimgan to Toyunduk-Kyzyltau align with the regional stress field governed by the Talas-Ferghana fault, underscoring the influence of inherited tectonic structures on basin development (Fig. 15C). Overall, the Jurassic sedimentary record is predominantly sourced from nearby backarc igneous rocks or recycled orogen. The Triassic granitoid batholiths in the North Pamir Terrane also partially contributed. These rocks were transported by hillslope mass wasting via alluvial fan and intermontane river systems.

CONCLUSIONS

By integrating new sedimentological, petrological, and geochronological data with published datasets on the Jurassic strata of the Tarim Basin, we have reached the following conclusions:

(1) In terms of provenance analysis, the southwestern Tarim Basin can be delineated into two tectonic domains: the Paleo-Tethys–North Pamir (Qimgan and Oytag) and the Paleo-Tethys–Western Kunlun Shan (Toyunduk-Kyzyltau and Fusha). The Jurassic clastic rocks of the Paleo-Tethys–North Pamir are inferred to have been predominantly sourced from the North Pamir Terrane, specifically from Triassic and late Paleozoic arc-related volcanic sequences, with minor contributions from the Triassic granitoid batholiths. In contrast, the Jurassic deposits of the Paleo-Tethys–Western Kunlun Shan domain are thought to have been largely derived from the North Kunlun–South Kunlun terranes, which include early Paleozoic collisional granitoid

batholiths and Proterozoic metamorphic crystalline basement.

(2) The well-preserved Triassic volcanic lithics within the Jurassic deposits of the Qimgan-Oytag sections are indicative of a Triassic backarc volcanic event linked to the Paleo-Tethys subduction, supporting the hypothesis of such activity in the northeastern Chinese Pamir region. These volcanic rocks served as the principal source of the Jurassic deposits.

(3) The Jurassic rifting observed in the Qimgan-Oytag region may be attributed to the tectonic inheritance of Triassic backarc extension, while from the perspective of the driving mechanism of regional extension, the rifting in the Toyunduk-Kyzyltau and Fusha regions is more likely interpreted as postcollisional extension driven by isostatic rebound.

REFERENCES CITED

Aminov, J., Ding, L., Mamadjonov, Y., Dupont-Nivet, G., Aminov, J., Zhang, L.Y., Yoqubov, S., Aminov, J., and Abdulov, S., 2017, Pamir Plateau formation and crustal thickening before the India–Asia collision inferred from dating and petrology of the 110–92 Ma Southern Pamir volcanic sequence: Gondwana Research, v. 51, p. 310–326, https://doi.org/10.1016/j.gr.2017.08.003.

Aminov, J., Roperch, P., Dupont-Nivet, G., Cordier, C., Guillot, S., Glodny, J., Timmerman, M.J., Sudo, M., Ruffet, G., Wilke, M., Lagroix, F., Lin, D., and Mamadjanov, Y., 2023, Contractional deformation between extensional dome exhumation in Central Pamir at 17–15 Ma constrained by metamorphic and paleomagnetic data from the Bartang volcanic rocks, Tajikistan: Tectonophysics, v. 868, https://doi.org/10.1016/j.tecto.2023.230080.

Arnaud, N.O., 1992, Apport de la thermochronologie ^{40}Ar/^{39}Ar sur feldspath potassique à la connaissance de la tectonique Cenozoique d'Asie: Étude des mécanismes d'accomodation de la collision continentale [Ph.D. thesis]: Clermont-Ferrand, France, University of Clermont-Ferrand, 161 p.

Bazhenov, M.L., 1996, Permo-Triassic paleomagnetism of the North Pamir: Tectonic implications: Earth and Planetary Science Letters, v. 142, p. 109–120, https://doi.org/10.1016/0012-821X(96)00090-8.

Bershaw, J., Garzione, C.N., Schoenbohm, L., Gehrels, G., and Tao, L., 2012, Cenozoic evolution of the Pamir

Plateau based on stratigraphy, zircon provenance, and stable isotopes of foreland basin sediments at Oytag (Wuyitake) in the Tarim Basin (West China): Journal of Asian Earth Sciences, v. 44, p. 136–148, https://doi.org/10.1016/j.jseaes.2011.04.020.

Blaise, J., Bordet, P., Lang, J., De, L.A.F., Leutwein, F., and Sonet, J., 1970, Mesures géochronologiques de quelques roches cristallines d'Afghanistan central: Comptes Rendus Hebdomadaires des Séances de l'Académie des Sciences, v. 270, p. 2772–2775.

Blayney, T., Najman, Y., Dupont-Nivet, G., Carter, A., Millar, I., Garzanti, E., Sobel, E.R., Rittner, M., Andò, S., Guo, Z., and Vezzoli, G., 2016, Indentation of the Pamirs with respect to the northern margin of Tibet: Constraints from the Tarim Basin sedimentary record: Tectonics, v. 35, p. 2345–2369, https://doi.org/10.1002/2016TC004222.

Bohor, B.F., and Triplehorn, D.M., 1993, Tonsteins: Altered Volcanic-Ash Layers in Coal-Bearing Sequences: Geological Society of America Special Paper 285, 44 p., https://doi.org/10.1130/SPE285-p1.

Budanov, V.I., 1993, Endogenous Formations of the Pamirs: Dushanbe, Tajikistan, Donish, 299 p.

Burtman, V.S., and Molnar, P., 1993, Geological and Geophysical Evidence for Deep Subduction of Continental Crust Beneath the Pamir: Geological Society of America Special Paper 281, 76 p., https://doi.org/10.1130/SPE281-p1.

Cao, K., Wang, G.C., Bernet, M., van der Beek, P., and Zhang, K.X., 2015, Exhumation history of the West Kunlun Mountains, northwestern Tibet: Evidence for a long-lived, rejuvenated orogen: Earth and Planetary Science Letters, v. 432, p. 391–403, https://doi.org/10.1016/j.epsl.2015.10.033.

Carrapa, B., Mustapha, F.S., Cosca, M., Gehrels, G., Schoenbohm, L.M., Sobel, E.R., DeCelles, P.G., Russell, J., and Goodman, P., 2014, Multisystem dating of modern river detritus from Tajikistan and China: Implications for crustal evolution and exhumation of the Pamir: Lithosphere, v. 6, p. 443–455, https://doi.org/10.1130/L360.1.

Castillo, P., Bahlburg, H., Fernandez, R., Fanning, C.M., and Berndt, J., 2022, The European continental crust through detrital zircons from modern rivers: Testing representativity of detrital zircon U-Pb geochronology: Earth-Science Reviews, v. 232, https://doi.org/10.1016/j.earscirev.2022.104145.

Cawood, P.A., Hawkesworth, C.J., and Dhuime, B., 2012, Detrital zircon record and tectonic setting: Geology, v. 40, p. 875–878, https://doi.org/10.1130/G32945.1.

Chapman, J.B., Carrapa, B., Ballato, P., DeCelles, P.G., Worthington, J., Oimahmadov, I., Gadoev, M., and Ketcham, R., 2017, Intracontinental subduction beneath the Pamir Mountains: Constraints from thermokinematic modeling of shortening in the Tajik fold-and-thrust belt: Geological Society of America Bulletin, v. 129, p. 1450–1471, https://doi.org/10.1130/B31730.1.

Chapman, J.B., Robinson, A.C., Carrapa, B., Villarreal, D., Worthington, J., DeCelles, P.G., Kapp, P., Gadoev, M., Oimahmadov, I., and Gehrels, G., 2018a, Cretaceous shortening and exhumation history of the South Pamir terrane: Lithosphere, v. 10, p. 494–511, https://doi.org/10.1130/L691.1.

Chapman, J.B., Scoggin, S.H., Kapp, P., Carrapa, B., Ducea, M.N., Worthington, J., Oimahmadov, I., and Gadoev, M., 2018b, Mesozoic to Cenozoic magmatic history of the Pamir: Earth and Planetary Science Letters, v. 482, p. 181–192, https://doi.org/10.1016/j.epsl.2017.10.041.

Corfu, F., Hanchar, J.M., Hoskin, P.W.O., and Kinny, P., 2003, Atlas of zircon textures: Reviews in Mineralogy and Geochemistry, v. 53, p. 469–500, https://doi.org/10.2113/0530469.

Cowgill, E., 2009, Cenozoic right-slip faulting along the eastern margin of the Pamir Salient, Northwestern China: Geological Society of America Bulletin, v. 122, p. 145–161, https://doi.org/10.1130/B26520.1.

Cowgill, E., Yin, A., Harrison, T.M., and Wang, X.F., 2003, Reconstruction of the Altyn Tagh fault based on U-Pb geochronology: Role of back thrusts, mantle sutures, and heterogeneous crustal strength in forming the Tibetan Plateau: Journal of Geophysical Research: Solid Earth, v. 108, https://doi.org/10.1029/2002JB002080.

Ding, L., Yang, D., Cai, F.L., Pullen, A., Kapp, P., Gehrels, G.E., Zhang, L.Y., Zhang, Q.H., Lai, Q.Z., Yue, Y.H., and Shi, R.D., 2013, Provenance analysis of the Mesozoic Hoh-Xil-Songpan-Ganzi turbidites in northern Tibet: Implications for the tectonic evolution of the eastern Paleo-Tethys Ocean: Tectonics, v. 32, p. 34–48, https://doi.org/10.1002/tect.20013.

Faisal, S., Larson, K.P., King, J., and Cottle, J.M., 2016, Rifting, subduction and collisional records from pluton petrogenesis and geochronology in the Hindu Kush, NW Pakistan: Gondwana Research, v. 35, p. 286–304, https://doi.org/10.1016/j.gr.2015.05.014.

Fang, W.X., Wang, L., Guo, Y.Q., Li, T.C., Jia, R.X., and Liu, Z.R., 2018, Tectonic patterns in the Sarekebayi apart-pull basin and their ore-controlling regularities for the Sareke glutenite-type copper deposit in Xinjiang, China: Earth Science Frontiers (Dixue Qianyuan), v. 25, p. 240–259.

Folk, R.L., 1980, Petrology of Sedimentary Rocks: Austin, Texas, Hemphill Publishing Co., 185 p.

Galloway, W.E., 1974, Deposition and diagenetic alteration of sandstone in northeast Pacific arc-related basins: Implications for graywacke genesis: Geological Society of America Bulletin, v. 85, p. 379–390, https://doi.org/10.1130/0016-7606(1974)85<379:DADAOS>2.0.CO;2.

Garzanti, E., 2019, Petrographic classification of sand and sandstone: Earth-Science Reviews, v. 192, p. 545–563, https://doi.org/10.1016/j.earscirev.2018.12.014.

Garzanti, E., Resentini, A., Vezzoli, G., Andò, S., Malusà, M.G., Padoan, M., and Paparella, P., 2010, Detrital fingerprints of fossil continental-subduction zones (axial belt provenance, European Alps): The Journal of Geology, v. 118, p. 341–362, https://doi.org/10.1086/652720.

Gawthorpe, R.L., and Leeder, M.R., 2000, Tectono-sedimentary evolution of active extensional basins: Basin Research, v. 12, p. 195–218, https://doi.org/10.1111/j.1365-2117.2000.00121.x.

Gibbons, A.D., Zahirovic, S., Müller, R.D., Whittaker, J.M., and Yatheesh, V., 2015, A tectonic model reconciling evidence for the collisions between India, Eurasia and intra-oceanic arcs of the central–eastern Tethys: Gondwana Research, v. 28, p. 451–492, https://doi.org/10.1016/j.gr.2015.01.001.

Girardeau, J., Marcoux, J., and Montenat, C., 1989, The Neo-Cimmerian Ophiolite Belt in Afghanistan and Tibet: Comparison and Evolution, in Şengör, A.M.C., ed., Tectonic Evolution of the Tethyan Region: Dordrecht, Netherlands, Springer, NATO ASI Series, v. 259, p. 477–504, https://doi.org/10.1007/978-94-009-2253-2_19.

Glazer, A., Avigad, D., Morag, N., and Gerdes, A., 2023, Tracing Oligocene–Miocene source-to-sink systems in the Deep Levant Basin: A sandstone provenance study: Geological Society of America Bulletin, v. 136, p. 1587–1604, https://doi.org/10.1130/B36864.1.

Golonka, J., and Bocharova, N.Y., 2000, Hot spot activity and the break-up of Pangea: Palaeogeography, Palaeoclimatology, Palaeoecology, v. 161, p. 49–69, https://doi.org/10.1016/S0031-0182(00)00117-6.

Graham, S.A., Hendrix, M.S., Wang, L.B., and Carroll, A.R., 1993, Collisional successor basins of western China: Impact of tectonic inheritance on sand composition: Geological Society of America Bulletin, v. 105, p. 323–344, https://doi.org/10.1130/0016-7606(1993)105<0323:CSBOWC>2.3.CO;2.

Grant, M.L., Wilde, S.A., Wu, F., and Yang, J., 2009, The application of zircon cathodoluminescence imaging, Th–U–Pb chemistry and U–Pb ages in interpreting discrete magmatic and high-grade metamorphic events in the North China Craton at the Archean/Proterozoic boundary: Chemical Geology, v. 261, p. 155–171, https://doi.org/10.1016/j.chemgeo.2008.11.002.

Hacker, B.R., Ratschbacher, L., Rutte, D., Stearns, M.A., Malz, N., Stübner, K., Kylander-Clark, A.R., Pfänder, J.A., and Everson, A., 2017, Building the Pamir–Tibet Plateau—Crustal stacking, extensional collapse, and lateral extrusion in the Pamir: 3. Thermobarometry and petrochronology of deep Asian crust: Tectonics, v. 36, p. 1743–1766, https://doi.org/10.1002/2017TC004488.

Hendrix, M.S., Graham, S.A., Carroll, A.R., Sobel, E.R., McKnight, C.L., Schulein, B.J., and Wang, Z.X., 1992, Sedimentary record and climatic implications of recurrent deformation in the Tian Shan: Evidence from Mesozoic strata of the North Tarim, South Junggar, and Turpan basins, Northwest China: Geological Society of America Bulletin, v. 104, p. 53–79, https://doi.org/10.1130/0016-7606(1992)104<0053:SRACIO>2.3.CO;2.

Henry, D.J., and Dutrow, B.L., 1996, Chapter 10. Metamorphic tourmaline and its petrologic applications, in Anovitz, L.M., and Grew, E.S., eds., Boron: Reviews in Mineralogy, v. 33, p. 503–558, https://doi.org/10.1515/9781501509223-012.

Huangfu, X.K., 2018, Geochemical characteristics and metallogenic mechanism of copper polymetallic deposit in Kungaishan mountain [M.S. thesis]: Beijing, China University of Geosciences, 87 p.

Hubert, J.F., 1962, A zircon-tourmaline-rutile maturity index and the interdependence of the composition of heavy mineral assemblages with the gross composition and texture of sandstones: Journal of Sedimentary Research, v. 32, p. 440–450, https://doi.org/10.1306/74D70CE5-2B21-11D7-8648000102C1865D.

Imrecke, D.B., Robinson, A.C., Owen, L.A., Chen, J., Schoenbohm, L.M., Hedrick, K.A., Lapen, T.J., Li, W.Q., and Yuan, Z.D., 2019, Mesozoic evolution of the eastern Pamir: Lithosphere, v. 11, p. 560–580, https://doi.org/10.1130/L1017.1.

Ji, W.H., Chen, S.J., Li, R.S., He, S.P., Zhao, Z.M., and Pan, X.P., 2017, The origin of Carboniferous-Permian magmatic rocks in Oytag area, West Kunlun: Back-arc basin?: Acta Petrologica Sinica (Yanshi Xuebao), v. 34, p. 2393–2409.

Ji, W.Q., Wu, F.Y., Wang, J.M., Liu, X.C., Liu, Z.C., Zhang, Z., Cao, W., Wang, J.G., and Zhang, C., 2020, Early evolution of Himalayan Orogenic Belt and generation of middle Eocene magmatism: Constraint from Haweng Granodiorite Porphyry in the Tethyan Himalaya: Frontiers of Earth Science, v. 8, https://doi.org/10.3389/feart.2020.00236.

Jiang, Y.H., Liao, S.Y., Yang, W.Z., and Shen, W.Z., 2008, An island arc origin of plagiogranites at Oytag, western Kunlun orogen, Northwest China: SHRIMP zircon U–Pb chronology, elemental and Sr–Nd–Hf isotopic geochemistry and Paleozoic tectonic implications: Lithos, v. 106, p. 323–335, https://doi.org/10.1016/j.lithos.2008.08.004.

Jiang, Y.H., Jia, R.Y., Liu, Z., Liao, S.Y., Zhao, P., and Zhou, Q., 2013, Origin of middle Triassic high-K calc-alkaline granitoids and their potassic microgranular enclaves from the western Kunlun orogen, Northwest China: A record of the closure of Paleo-Tethys: Lithos, v. 156–159, p. 13–30, https://doi.org/10.1016/j.lithos.2012.10.004.

Johnsson, M.J., 1993, The system controlling the composition of clastic sediments, in Johnsson, M.J., and Basu, A., eds., Processes Controlling the Composition of Clastic Sediments: Geological Society of America Special Paper 284, p. 1–20, https://doi.org/10.1130/SPE284-p1.

Kapp, P., DeCelles, P.G., Gehrels, G.E., Heizler, M., and Ding, L., 2007, Geological records of the Lhasa-Qiangtang and Indo-Asian collisions in the Nima area of Central Tibet: Geological Society of America Bulletin, v. 119, p. 917–933, https://doi.org/10.1130/B26033.1.

Kellett, D.A., and Grujic, D., 2012, New insight into the South Tibetan detachment system: Not a single progressive deformation: Tectonics, v. 31, https://doi.org/10.1029/2011TC002957.

Li, G., Sandiford, M., Fang, A., Kohn, B., Sandiford, D., Fu, B., Zhang, T., Cao, Y., and Chen, F., 2019a, Multi-stage exhumation history of the West Kunlun orogen and the amalgamation of the Tibetan Plateau: Earth and Planetary Science Letters, v. 528, https://doi.org/10.1016/j.epsl.2019.115833.

Li, H., Li, H., Gao, B., Wang, W., and Liu, C., 2017, Study on pore characteristics and microstructure of sandstones with different grain sizes: Journal of Applied Geophysics, v. 136, p. 364–371, https://doi.org/10.1016/j.jappgeo.2016.11.015.

Li, T., Chen, Z., Chen, J., Thompson Jobe, J.A., Burbank, D.W., Li, Z., He, X., Zheng, W., Zhang, P., and Zhang, B., 2019b, Along-strike and downdip segmentation of the Pamir frontal thrust and its association with the

1985 M$_w$ 6.9 Wuqia earthquake: Journal of Geophysical Research: Solid Earth, v. 124, p. 9890–9919, https://doi.org/10.1029/2019JB017319.

Li, T.F., and Zhang, J.X., 2014, Zircon LA-ICPMS U-Pb ages of websterite and basalt in Kudi ophiolite and the implications, West Kunlun: Acta Petrologica Sinica (Yanshi Xuebao), v. 30, p. 2393–2401.

Li, Y., Robinson, A.C., Zucali, M., Gadoev, M., Oimuhammadzoda, I., Lapen, T.J., and Carrapa, B., 2022, Mesozoic tectonic evolution in the Kurgovat-Vanch Complex, NW Pamir: Tectonics, v. 41, https://doi.org/10.1029/2021TC007180.

Li, Y.P., Robinson, A.C., Gadoev, M., and Oimuhammadzoda, I., 2020, Was the Pamir salient built along a late Paleozoic embayment on the southern Asian margin?: Earth and Planetary Science Letters, v. 550, https://doi.org/10.1016/j.epsl.2020.116554.

Liati, A., Gebauer, D., and Wysoczanski, R., 2002, U–Pb SHRIMP-dating of zircon domains from UHP garnet-rich mafic rocks and late pegmatoids in the Rhodope zone (N Greece); evidence for Early Cretaceous crystallization and Late Cretaceous metamorphism: Chemical Geology, v. 184, p. 281–299, https://doi.org/10.1016/S0009-2541(01)00367-9.

Linnemann, U., Ouzegane, K., Drareni, A., Hofmann, M., Becker, S., Gärtner, A., and Sagawe, A., 2011, Sands of West Gondwana: An archive of secular magmatism and plate interactions—A case study from the Cambro-Ordovician section of the Tassili Ouan Ahaggar (Algerian Sahara) using U–Pb–LA-ICP-MS detrital zircon ages: Lithos, v. 123, p. 188–203, https://doi.org/10.1016/j.lithos.2011.01.010.

Liu, L.T., Chen, J., and Li, T., 2017, Detrital zircon U-Pb dating of modern rivers' deposits in Pamir, South Tian Shan and their convergence zone: Dizhen Dizhi, v. 39, p. 497–516, https://doi.org/10.3969/j.issn.0253-4967.2017.03.005.

Liu, X.Q., Zhang, C.L., Zou, H., Wang, Q., Hao, X.S., Zhao, H.X., and Ye, X.T., 2020, Triassic–Jurassic granitoids and pegmatites from western Kunlun-Pamir Syntax: Implications for the paleo-Tethys evolution at the northern margin of the Tibetan Plateau: Lithosphere, v. 2020, https://doi.org/10.2113/2020/7282037.

Liu, X.Q., Zhang, C.L., Zou, H., and Ye, X.T., 2023, Diverse metavolcanic sequences in the Cambrian accretionary complex at the Pamir Syntax: Implications for tectonic evolution from Proto-Tethys to Paleo-Tethys: Journal of Asian Earth Sciences, v. 241, https://doi.org/10.1016/j.jseaes.2022.105481.

Liu, Z., Jiang, Y.H., Jia, R.Y., Zhao, P., and Zhou, Q., 2015, Origin of Late Triassic high-k calc-alkaline granitoids and their potassic microgranular enclaves from the western Tibet Plateau, Northwest China: Implications for paleo-Tethys evolution: Gondwana Research, v. 27, p. 326–341, https://doi.org/10.1016/j.gr.2013.09.022.

Liu, Z.S., 2002, Jurassic palynofloral provinces of Tarim Basin: Dicengxue Zazhi, v. 26, p. 18–26.

Lukens, C.E., Carrapa, B., Singer, B.S., and Gehrels, G., 2012, Miocene exhumation of the Pamir revealed by detrital geothermochronology of Tajik rivers: Tectonics, v. 31, https://doi.org/10.1029/2011TC003040.

Luo, H., Xiong, F., Huang, H., Yan, D., Zhang, D., Li, F., and Hou, M., 2024, Provenance of Late Carboniferous–Triassic clastic rocks in the Western Kunlun orogenic belt, western China: Implications for the tectonic evolution of the Paleo-Tethys Ocean: Journal of Asian Earth Sciences, v. 267, https://doi.org/10.1016/j.jseaes.2024.106162.

Matte, P., Tapponnier, P., Arnaud, N., Bourjot, L., Avouac, J.P., Vidal, Ph., Liu, Q., Pan, Y.S., and Wang, Y., 1996, Tectonics of Western Tibet, between the Tarim and the Indus: Earth and Planetary Science Letters, v. 142, p. 311–330, https://doi.org/10.1016/0012-821X(96)00086-6.

Mattern, F., and Schneider, W., 2000, Suturing of the Proto- and Paleo-Tethys oceans in the western Kunlun (Xinjiang, China): Journal of Asian Earth Sciences, v. 18, p. 637–650, https://doi.org/10.1016/S1367-9120(00)00011-0.

McFadden, P.L., Ma, X.H., McElhinny, M.W., and Zhang, Z.K., 1988, Permo-Triassic magnetostratigraphy in China: Northern Tarim: Earth and Planetary Science

Letters, v. 87, p. 152–160, https://doi.org/10.1016/0012-821X(88)90071-4.

Metcalfe, I., 2021, Multiple Tethyan ocean basins and orogenic belts in Asia: Gondwana Research, v. 100, p. 87–130, https://doi.org/10.1016/j.gr.2021.01.012.

Morton, A.C., and Hallsworth, C., 1994, Identifying provenance-specific features of detrital heavy mineral assemblages in sandstones: Sedimentary Geology, v. 90, p. 241–256, https://doi.org/10.1016/0037-0738(94)90041-8.

Mu, S.L., 2016, Volcanic rocks tectonic environments and metallogenesis of typical mineral deposits in Kungai Mountains, West Kunlun [Ph.D. thesis]: Guangzhou, China, University of Chinese Academy of Sciences, 186 p.

Panca, F., Bahlburg, H., Cárdenas, J., Berndt, J., Lünsdorf, N.K., and Gerdes, A., 2024, Sedimentology, geochronology and provenance of the Late Permian and Triassic Mitu Group in Peru—The evolution of continental facies along a transform margin: Basin Research, v. 36, https://doi.org/10.1111/bre.12864.

Paton, C., Woodhead, J.D., Hellstrom, J.C., Hergt, J.M., Greig, A., and Maas, R., 2010, Improved laser ablation U–Pb zircon geochronology through robust downhole fractionation correction: Geochemistry, Geophysics, Geosystems, v. 11, https://doi.org/10.1029/2009GC002618.

Pittman, E.D., 1970, Plagioclase feldspar as an indicator of provenance in sedimentary rocks: Journal of Sedimentary Research, v. 40, p. 591–598, https://doi.org/10.1306/74D71FDC-2B21-11D7-8648000102C1865D.

Rembe, J., Sobel, E.R., Kley, J., Zhou, R., Thiede, R., and Chen, J., 2021, The Carboniferous arc of the North Pamir: Lithosphere, v. 2021, https://doi.org/10.2113/2021/6697858.

Rembe, J., Sobel, E.R., Kley, J., Terbishalieva, B., Musiol, A., Chen, J., and Zhou, R., 2022, Geochronology, geochemistry, and geodynamic implications of Permo-Triassic back-arc basin successions in the North Pamir, Central Asia: Lithosphere, v. 2022, https://doi.org/10.2113/2022/7514691.

Rittner, M., Vermeesch, P., Carter, A., Bird, A., Stevens, T., Garzanti, E., Andò, S., Vezzoli, G., Dutt, R., Xu, Z., and Lu, H., 2016, The provenance of Taklamakan Desert Sand: Earth and Planetary Science Letters, v. 437, p. 127–137, https://doi.org/10.1016/j.epsl.2015.12.036.

Robinson, A.C., 2015, Mesozoic tectonics of the Gondwanan terranes of the Pamir Plateau: Journal of Asian Earth Sciences, v. 102, p. 170–179, https://doi.org/10.1016/j.jseaes.2014.09.012.

Robinson, A.C., Yin, A., Manning, C.E., Harrison, T.M., Zhang, S.H., and Wang, X.F., 2007, Cenozoic evolution of the eastern Pamir: Implications for strain-accommodation mechanisms at the western end of the Himalayan-Tibetan orogen: Geological Society of America Bulletin, v. 119, p. 882–896, https://doi.org/10.1130/B25981.1.

Rutte, D., Ratschbacher, L., Schneider, S., Stübner, K., Stearns, M.A., Gulzar, M.A., and Hacker, B.R., 2017, Building the Pamir-Tibetan Plateau—Crustal stacking, extensional collapse, and lateral extrusion in the Central Pamir: 1. Geometry and kinematics: Tectonics, v. 36, p. 342–384, https://doi.org/10.1002/2016TC004293.

Salikhov, F.S., and Sakiev, K.S., 2014, Stages of sedimentation in the Permian-Triassic North Pamirs: Bulletin of the Institute of the National Academy of Sciences of the Kyrgyz Republic, v. 4, p. 79–86.

Saylor, J.E., and Sundell, K.E., 2016, Quantifying comparison of large detrital geochronology data sets: Geosphere, v. 12, p. 203–220, https://doi.org/10.1130/GES01237.1.

Schmidt, J., Hacker, B.R., Ratschbacher, L., Stübner, K., Stearns, M., Kylander-Clark, A., Cottle, J.M., Alexander, A., Webb, G., Gehrels, G., and Minaev, V., 2011, Cenozoic deep crust in the Pamir: Earth and Planetary Science Letters, v. 312, p. 411–421, https://doi.org/10.1016/j.epsl.2011.10.034.

Schwab, M., Ratschbacher, L., Siebel, W., McWilliams, M., Minaev, V., Lutkov, V., Chen, F., Stanek, K., Nelson, B., Frisch, W., and Wooden, J.L., 2004, Assembly of the Pamirs: Age and origin of magmatic belts from the

southern Tien Shan to the southern Pamirs and their relation to Tibet: Tectonics, v. 23, https://doi.org/10.1029/2003TC001583.

Siehl, A., 2017, Structural setting and evolution of the Afghan orogenic segment–A Review, *in* Brunett, M.F., et al., eds., Geological Evolution of Central Asian Basins and the Western Tien Shan Range: Geological Society, London, Special Publication 427, p. 57–88, https://doi.org/10.1144/SP427.8.

Sláma, J., Košler, J., Condon, D.J., Crowley, J.L., Gerdes, A., Hanchar, J.M., Horstwood, M.S.A., Morris, G.A., Nasdala, L., Norberg, N., Schaltegger, U., Schoene, B., Tubrett, M.N., and Whitehouse, M.J., 2008, Plešovice zircon—A new natural reference material for U-Pb and HF isotopic microanalysis: Chemical Geology, v. 249, p. 1–35, https://doi.org/10.1016/j.chemgeo.2007.11.005.

Sobel, E.R., 1999, Basin analysis of the Jurassic–lower Cretaceous Southwest Tarim Basin, Northwest China: Geological Society of America Bulletin, v. 111, p. 709–724, https://doi.org/10.1130/0016-7606(1999)111<0709:BAOTJL>2.3.CO;2.

Sobel, E.R., Chen, J., Schoenbohm, L.M., Thiede, R., Stockli, D.F., Sudo, M., and Strecker, M.R., 2013, Oceanic-style subduction controls late Cenozoic deformation of the northern Pamir orogen: Earth and Planetary Science Letters, v. 363, p. 204–218, https://doi.org/10.1016/j.epsl.2012.12.009.

Song, Z.H., Zhang, C.L., Sargazi, M., Hussain, Z., Liu, X.Q., Ye, X.T., and Wang, H.R., 2024, Carboniferous bimodal volcanic sequences along the northeastern Pamir: Evidence for back-arc extension due to northward subduction of the Paleo-Tethys: Geological Society of America Bulletin, v. 136, p. 3769–3785, https://doi.org/10.1130/B37153.1.

Stevens, T., Carter, A., Watson, T.P., Vermeesch, P., Andò, S., Bird, A.F., Lu, H., Garzanti, E., Cottam, M.A., and Sevastjanova, I., 2013, Genetic linkage between the Yellow River, the Mu Us desert and the Chinese Loess Plateau: Quaternary Science Reviews, v. 78, p. 355–368, https://doi.org/10.1016/j.quascirev.2012.11.032.

Tang, G.J., Cawood, P.A., Wyman, D.A., Dan, W., Wang, Q., and Yang, Y.N., 2021, The missing magmatic arc in a long-lived ocean from the Western Kunlun–Pamir Paleo-Tethys realm: Geophysical Research Letters, v. 48, https://doi.org/10.1029/2021GL095192.

Tian, Z., Chai, G., and Kang, Y., 1989, Tectonic evolution of the Tarim Basin, in Chinese Sedimentary Basins, *in* Zhu, X., ed., Sedimentary Basins of the World: Amsterdam, Elsevier, p. 33–42.

Torsvik, T.H., and Cocks, L.R., 2013, Gondwana from top to base in space and time: Gondwana Research, v. 24, p. 999–1030, https://doi.org/10.1016/j.gr.2013.06.012.

Vermeesch, P., 2013, Multi-sample comparison of detrital age distributions: Chemical Geology, v. 341, p. 140–146, https://doi.org/10.1016/j.chemgeo.2013.01.010.

Villarreal, D.P., Robinson, A.C., Carrapa, B., Worthington, J., Chapman, J.B., Oimahmadov, I., Gadoev, M., and MacDonald, B., 2020, Evidence for Late Triassic crustal suturing of the Central and Southern Pamir: Journal of Asian Earth Sciences: X, v. 3, https://doi.org/10.1016/j.jaesx.2019.100024.

von Eynatten, H., and Dunkl, I., 2012, Assessing the sediment factory: The role of single grain analysis: Earth-Science Reviews, v. 115, p. 97–120, https://doi.org/10.1016/j.earscirev.2012.08.001.

Wang, J., Hattori, K., Liu, J.G., Song, Y., Gao, Y.B., and Zhang, H., 2017, Shoshonitic- and adakitic magmatism of the early Paleozoic age in the Western Kunlun Orogenic Belt, NW China: Implications for the early evolution of the northwestern Tibetan Plateau: Lithos, v. 286–287, p. 345–362, https://doi.org/10.1016/j.lithos.2017.06.013.

Wang, S.F., Tang, W.K., Liu, Y.D., Liu, X.H., and Yao, X., 2020, Rushan-Pshart Paleo-Tethyan suture deduced from geochronological, geochemical, and Sr–Nd–Hf isotopic characteristics of granitoids in Pamir: Lithos, v. 364–365, https://doi.org/10.1016/j.lithos.2020.105549.

Wei, X., Wang, H., Zhang, X., Dong, R., Zhu, S., Xing, C., Li, P., Yan, Q., and Zhou, K., 2023, Petrogenesis and geological significance of Late-Triassic high-Mg

diorite from eastern West Kunlun: Geochimica (Diqiu Huaxue), v. 47, no. 4, p. 363–379.

Weltje, G.J., and von Eynatten, H., 2004, Quantitative provenance analysis of sediments: An introduction, *in* Weltje, G.J., and von Eynatten, H., eds., Quantitative Provenance Analysis of Sediments: Sedimentary Geology, v. 171, p. 1–11.

Williams, I.S., 2001, Response of detrital zircon and monazite, and their U–Pb isotopic systems, to regional metamorphism and host-rock partial melting, Cooma Complex, southeastern Australia: Australian Journal of Earth Sciences, v. 48, p. 557–580, https://doi.org/10.1046/j.1440-0952.2001.00883.x.

Windley, B., 1983, Metamorphism and tectonics of the Himalaya: Journal of the Geological Society, v. 140, p. 849–865, https://doi.org/10.1144/gsjgs.140.6.0849.

Wolf, S.G., Huismans, R.S., Braun, J., and Yuan, X.P., 2022, Topography of mountain belts controlled by rheology and surface processes: Nature, v. 606, p. 516–521, https://doi.org/10.1038/s41586-022-04700-6.

Wolfart, R., and Wittekindt, H., 1980, Geologie von Afghanistan: Berlin, Borntraeger, 500 p.

Wu, F.Y., Wan, B., Zhao, L., Xiao, W.J., and Zhu, R.X., 2020, Tethyan geodynamics: Acta Petrologica Sinica (Yanshi Xuebao), v. 36, p. 1627–1674, https://doi.org/10.18654/1000-0569/2020.06.01.

Wu, H.X., 2017, Characteristics of paleostructure in the mountain front region of south-western Tarim Basin and its control of Jurassic–Cretaceous deposition [M.S. thesis]: Hangzhou, China, Zhejiang University, 78 p.

Wu, H.X., Cheng, X.G., Chen, H.L., Chen, C., Dilek, Y., Shi, J., Zeng, C.M., Li, C.Y., Zhang, W., Zhang, Y.Q., Lin, X.B., and Zhang, F.Q., 2021, Tectonic switch from Triassic contraction to Jurassic-Cretaceous extension in the Western Tarim Basin, Northwest China: New insights into the evolution of the Paleo-Tethyan Orogenic Belt: Frontiers of Earth Science, v. 9, https://doi.org/10.3389/feart.2021.636383.

Wu, H.X., Chen, H.L., Zuza, A.V., Dilek, Y., Qiu, D.W., Lu, Q.Y., Zhang, F.Q., Cheng, X.G., and Lin, X.B., 2025, Switching extensional and contractional tectonics in the West Kunlun Mountains during the Jurassic period: Responses to the Neo-Tethyan Geodynamics along the Eurasian margin: Solid Earth, v. 16, p. 155–177, https://doi.org/10.5194/se-16-155-2025.

Xiao, L., Zhang, H.F., Clemens, J.D., Wang, Q.W., Kan, Z.Z., Wang, K.M., Ni, P.Z., and Liu, X.M., 2007, Late Triassic granitoids of the eastern margin of the Tibetan Plateau: Geochronology, petrogenesis and implications for tectonic evolution: Lithos, v. 96, p. 436–452, https://doi.org/10.1016/j.lithos.2006.11.011.

Xiao, W.J., Windley, B.F., Chen, H.L., Zhang, G.C., and Li, J.L., 2002, Carboniferous–Triassic subduction and accretion in the western Kunlun, China: Implications for the collisional and accretionary tectonics of the northern Tibetan Plateau: Geology, v. 30, p. 295–298, https://doi.org/10.1130/0091-7613(2002)030<0295:CTSAAI>2.0.CO;2.

Xiao, W.J., Han, F.L., Windley, B.F., Yuan, C., Zhou, H., and Li, J.L., 2003, Multiple accretionary orogenesis and episodic growth of continents: Insights from the Western Kunlun Range, Central Asia: International Geology Review, v. 45, p. 303–328, https://doi.org/10.2747/0020-6814.45.4.303.

Xu, Q., Zhao, J.M., Yuan, X.H., Liu, H.B., Ju, C.H., Schurr, B., and Bloch, W., 2021, Deep crustal contact between the Pamir and Tarim Basin deduced from receiver functions: Geophysical Research Letters, v. 48, https://doi.org/10.1029/2021GL093271.

Xu, W., Dong, Y.S., Zhang, X.Z., Deng, M.R., and Zhang, L., 2016, Petrogenesis of high-Ti mafic dykes from Southern Qiangtang, Tibet: Implications for a ca. 290 Ma large igneous province related to the early Permian rifting of Gondwana: Gondwana Research, v. 36, p. 410–422, https://doi.org/10.1016/j.gr.2015.07.016.

Xu, W., Liu, F.L., and Dong, Y.S., 2020, Cambrian to Triassic geodynamic evolution of Central Qiangtang, Tibet: Earth-Science Reviews, v. 201, https://doi.org/10.1016/j.earscirev.2020.103083.

Yan, Q.H., Wang, H., Chi, G.X., Wang, Q., Hu, H., Zhou, K.L., and Zhang, X.Y., 2022, Recognition of a 600-km-long Late Triassic rare metal (Li-Rb-Be-Nb-Ta) pegmatite belt in the western Kunlun Orogenic Belt, western China: Economic Geology, v. 117, p. 213–236, https://doi.org/10.5382/econgeo.4858.

Yang, W., Fu, L., Wu, C.D., Song, Y., Jiang, Z.X., Luo, Q., Zhang, Z.Y., Zhang, C., and Zhu, B., 2018, U–Pb ages of detrital zircon from Cenozoic sediments in the south-western Tarim Basin, NW China: Implications for Eocene–Pliocene source-to-sink relations and new insights into Cretaceous–Paleogene magmatic sources: Journal of Asian Earth Sciences, v. 156, p. 26–40, https://doi.org/10.1016/j.jseaes.2018.01.010.

Yin, A., and Harrison, T.M., 2000, Geologic evolution of the Himalayan-Tibetan orogen: Annual Review of Earth and Planetary Sciences, v. 28, p. 211–280, https://doi.org/10.1146/annurev.earth.28.1.211.

Yin, J.Y., Xiao, W.J., Sun, M., Chen, W., Yuan, C., Zhang, Y.Y., Wang, T., Du, Q., Wang, X.S., and Xia, X.P., 2020, Petrogenesis of Early Cambrian granitoids in the western Kunlun orogenic belt, Northwest Tibet: Insight into early stage subduction of the Proto-Tethys Ocean: Geological Society of America Bulletin, v. 132, p. 2221–2240, https://doi.org/10.1130/B35408.1.

Yuan, C., Sun, M., Zhou, M.F., Zhou, H., Xiao, W.J., and Li, J.L., 2002, Tectonic evolution of the West Kunlun: Geochronologic and geochemical constraints from Kudi granitoids: International Geology Review, v. 44, p. 653–669, https://doi.org/10.2747/0020-6814.44.7.653.

Zanchetta, S., Worthington, J., Angiolini, L., Leven, E. Ja., Villa, I.M., and Zanchi, A., 2018, The Bashgumbaz Complex (Tajikistan): Arc obduction in the Cimmerian orogeny of the Pamir: Gondwana Research, v. 57, p. 170–190, https://doi.org/10.1016/j.gr.2018.01.009.

Zha, X.F., Dong, Y.P., Gao, X.F., Ji, W.H., Liu, X.M., He, D.F., Li, P., Zhang, H.D., and Yang, C., 2022, The early Paleozoic Subashi ophiolite in the West Kunlun Orogenic Belt (northwestern Tibetan Plateau): Implication for the tectonic evolution of the Proto-Tethys: Journal of Asian Earth Sciences, v. 238, https://doi.org/10.1016/j.jseaes.2022.105388.

Zhang, C.L., Yu, H.F., Ye, H.M., Zhao, Y., and Zhang, D.S., 2006, Aoyitake plagiogranite in western Tarim Block, NW China: Age, geochemistry, petrogenesis and its tectonic implications: Science in China Series D: Earth Sciences, v. 49, p. 1121–1134, https://doi.org/10.1007/s11430-006-1121-y.

Zhang, C.L., Zou, H.B., Ye, X.T., and Chen, X.Y., 2018, A newly identified Precambrian terrane at the Pamir Plateau: The Archean basement and Neoproterozoic granitic intrusions: Precambrian Research, v. 304, p. 73–87, https://doi.org/10.1016/j.precamres.2017.11.006.

Zhang, C.L., Zou, H.B., Ye, X.T., and Chen, X.Y., 2019a, Tectonic evolution of the West Kunlun Orogenic Belt along the northern margin of the Tibetan Plateau: Implications for the assembly of the Tarim Terrane to Gondwana: Geoscience Frontiers, v. 10, p. 973–988, https://doi.org/10.1016/j.gsf.2018.05.006.

Zhang, Q.C., Li, Z.H., Wu, Z.H., Chen, X.H., Zhang, J.E., and Yang, Y., 2021, Subduction initiation of the western Proto-Tethys Ocean: New evidence from the Cambrian intra-oceanic forearc ophiolitic mélange in the western Kunlun Orogen, NW Tibetan Plateau: Geological Society of America Bulletin, v. 134, p. 145–159, https://doi.org/10.1130/B35922.1.

Zhang, S.J., Hu, X.M., and Garzanti, E., 2019b, Paleocene initial indentation and early growth of the Pamir as recorded in the western Tarim Basin: Tectonophysics, v. 772, https://doi.org/10.1016/j.tecto.2019.228207.

Zheng, J.P., and Dai, H.K., 2018, Subduction and retreating of the western Pacific plate resulted in lithospheric mantle replacement and coupled basin-mountain respond in the North China Craton: Science China Earth Sciences, v. 61, p. 406–424, https://doi.org/10.1007/s11430-017-9166-8.

Zheng, Y.L., Wang, G.H., Guo, Z.W., Liang, X., Yuan, G.L., Wang, H.D., Huang, B., and He, Y.D., 2015, The record of the Pan-African and the Indosinian tectono-thermal event in Qiangtang terrane, northern Tibet: Evidence from geochemical characteristics and U–Pb geochronology of the metamorphic complex in Ejiumai area: Acta Petrologica Sinica, v. 31, p. 1137–1152.

Zhong, D.K., Zhu, X.M., Wang, G.W., and Xie, Q.B., 2002, Paleoenvironments of Jurassic of Kashi Sag in Tarim Basin: Journal of Palaeogeography, v. 4, p. 47–54.

Zhu, G.Y., Su, J., Yang, H.J., Wang, Y., Fei, A.G., Liu, K.Y., Zhu, Y.F., Hu, J.F., and Zhang, B.S., 2013, Formation mechanisms of secondary hydrocarbon pools in the Triassic reservoirs in the northern Tarim Basin: Marine and Petroleum Geology, v. 46, p. 51–66, https://doi.org/10.1016/j.marpetgeo.2013.06.006.